

# MeerKAT view of Hickson Compact Groups:

## I. Data description and release

R. Ianjamasimanana<sup>1</sup>, L. Verdes-Montenegro<sup>1</sup>, A. Sorgho<sup>1</sup>, K. M. Hess<sup>2,3,1</sup>, M. G. Jones<sup>4</sup>, J. M. Cannon<sup>9</sup>, J. M. Solanes<sup>6,7</sup>, M. E. Cluver<sup>8</sup>, J. Moldón<sup>1</sup>, B. Namumba<sup>1</sup>, J. Román<sup>14</sup>, I. Labadie-García<sup>1</sup>, C.C. de la Casa<sup>1</sup>, S. Borthakur<sup>13</sup>, J. Wang<sup>5</sup>, R. García-Benito<sup>1</sup>, A. del Olmo<sup>1</sup>, J. Perea<sup>1</sup>, T. Wiegert<sup>1</sup>, M. Yun<sup>15</sup>, J. Garrido<sup>1</sup>, S. Sanchez-Expósito<sup>1</sup>, A. Bosma<sup>10</sup>, E. Athanassoula<sup>10</sup>, G. I. G. Józsa<sup>11,12</sup>, T.H. Jarrett<sup>16,17</sup>, C.K. Xu<sup>18,19</sup> O.M. Smirnov<sup>12,20</sup>

<sup>1</sup> Instituto de Astrofísica de Andalucía (CSIC), Glorieta de la Astronomía s/n, 18008 Granada, Spain  
e-mail: ianja@iaa.es

<sup>2</sup> Department of Space, Earth and Environment, Chalmers University of Technology, Onsala Space Observatory, 43992 Onsala, Sweden

<sup>3</sup> ASTRON, the Netherlands Institute for Radio Astronomy, Oude Hoogeveensedijk 4,7991 PD Dwingeloo, The Netherlands

<sup>4</sup> Steward Observatory, University of Arizona, 933 North Cherry Avenue, Rm. N204, Tucson, AZ 85721-0065, USA

<sup>5</sup> Kavli Institute for Astronomy and Astrophysics, Peking University, Beijing 100871, People's Republic of China

<sup>6</sup> Departament de Física Quàntica i Astrofísica, Universitat de Barcelona, C. Martí i Franquès 1, 08028, Barcelona, Spain

<sup>7</sup> Institut de Ciències del Cosmos (ICCUB), Universitat de Barcelona., C. Martí i Franquès 1, 08028, Barcelona, Spain

<sup>8</sup> Centre for Astrophysics and Supercomputing, Swinburne University of Technology, Hawthorn, VIC 3122, Australia

<sup>9</sup> Department of Physics & Astronomy, Macalester College, 1600 Grand Avenue, Saint Paul, MN 55105, USA

<sup>10</sup> Aix Marseille Univ, CNRS, CNES, LAM, Marseille, France

<sup>11</sup> Max-Planck Institut für Radioastronomie, Auf dem Hügel 69, 53121, Bonn, Germany

<sup>12</sup> Centre for Radio Astronomy Techniques and Technologies (RATT), Department of Physics and Electronics, Rhodes University, PO Box 94, Grahamstown 6140, South Africa

<sup>13</sup> School of Earth and Space Exploration, Arizona State University, 781 Terrace Mall, Tempe, AZ, 85287, USA

<sup>14</sup> Departamento de Física de la Tierra y Astrofísica, Universidad Complutense de Madrid, E-28040 Madrid, Spain

<sup>15</sup> Department of Astronomy, University of Massachusetts, Amherst, MA 01003, USA

<sup>16</sup> Department of Astronomy, University of Cape Town, Rondebosch, Cape Town 7700, South Africa

<sup>17</sup> Western Sydney University, Locked Bag 1797, Penrith South DC, NSW 1797, Australia

<sup>18</sup> Chinese Academy of Sciences South America Center for Astronomy, National Astronomical Observatories, CAS, Beijing, People's Republic of China

<sup>19</sup> National Astronomical Observatories, Chinese Academy of Sciences (NAOC), Beijing, People's Republic of China

<sup>20</sup> South African Radio Astronomy Observatory, Cape Town, 7925, South Africa

Received November 14, 2024; accepted February 03, 2025

### ABSTRACT

**Context.** Hickson Compact Groups (HCGs) are dense gravitationally-bound collections of 4-10 galaxies ideal for studying gas and star formation quenching processes.

**Aims.** We aim to understand the transition of HCGs from possessing complex H I tidal structures (so-called phase 2 groups) to a phase where galaxies have lost most or all their H I (phase 3). We also seek to detect diffuse H I gas that was previously missed by the Very Large Array (VLA).

**Methods.** We observed three phase 2 and three phase 3 HCGs with MeerKAT and reduced the data using the Containerized Automated Radio Astronomy Calibration (CARACal) pipeline. We produced data cubes, moment maps, integrated spectra, and compared our findings with previous VLA and Green Bank Telescope (GBT) observations.

**Results.** Compared with previous VLA observations, MeerKAT reveals much more extended tidal features in phase 2 and some new high surface brightness features in phase 3 groups. However, no diffuse H I component was found in phase 3 groups. We also detected many surrounding galaxies for both phase 2 and phase 3 groups, most of which are normal disk galaxies.

**Conclusions.** The difference between phase 2 and phase 3 groups is still substantial, supporting previous finding that the transition between the two phases must be abrupt.

**Key words.** galaxies:evolution – galaxies:groups – galaxies:interactions – galaxies:ISM

## 1. Introduction

Hickson Compact Groups (HCGs) are systems of typically four to ten groups of galaxies in close proximity to each other. They were first catalogued by Paul Hickson in 1982. On large scales,

they are located in low-density environment (Palumbo et al. 1995). Their galaxy members are characterised by low-velocity dispersion ( $\sim 200 \text{ km s}^{-1}$ , Hickson et al. 1992) but are separated by small distances like in the centre of clusters, making

HCGs an ideal case to study gas and star formation quenching processes. According to the evolutionary sequence proposed by Verdes-Montenegro et al. (2001), in phase 1, galaxies in HCGs have the majority of their neutral atomic hydrogen (H I) gas in the disk of the galaxies. In phase 2, gravitational interactions between member galaxies are thought to be the main driver in disrupting gas morphology and kinematics, displacing approximately 30% to 60% of the gas from the disks, and forming structures such as tidal tails and bridges. Phase 3 HCGs are divided into two subcategories. In phase 3a, most or all the gas is found in the form of intra-group clouds or tidal tails. In phase 3b, the H I in the groups forms a large cloud with a single peaked global profile and a single velocity gradient. However, Jones et al. (2023) questioned the existence of this latter phase, as subsequent studies found that only HCG 49, among the 72 HCGs analysed by Verdes-Montenegro et al. (2001), fit this classification. Jones et al. (2023) made a minor modification to the original evolutionary sequence of HCGs proposed by Verdes-Montenegro et al. (2001). The first modification concerns the threshold at which groups are classified as being phase 2 or phase 3. Jones et al. (2023) redefined phase 2 groups as those where 25% to 75% of the H I was associated with features not related to the disk of the galaxies. If more than 75% of the H I was associated with extended features, they classified the groups as phase 3. The second modification involved the elimination of the phase 3b classification and the introduction of phase 3c. They used this new designation scheme to specify HCGs that would have been classified as phase 1, but where only one galaxy among the group members was detected in H I. In fact, phase 3c groups are thought to be systems at a very late evolutionary stage but have recently acquired a new member galaxy. In this paper, we will use the modified classification scheme by Jones et al. (2023).

The H I content of HCGs have been the subject of many studies in the literature. Williams & Rood (1987) observed 51 HCGs using the NRAO 91 m and NAIC 305 m telescopes. They found that HCGs contain, on average, half as much H I as loose groups of similar optical morphology and luminosity types. Their H I mass is lower than the expected H I mass from their optical morphology and luminosity types. Huchtmeier (1997) used the Effelsberg 100-m telescope to observe 54 HCGs at 21 cm wavelength. They detected H I for 41 HCGs. The detection rate increased with the number of spiral galaxies in the groups. Huchtmeier (1997) expanded their study by incorporating the sample from Williams & Rood (1987), resulting in a total of 75 HCGs, including 61 detections and 14 upper limits. Huchtmeier (1997) observed many HI-deficient groups by comparing their integrated H I mass with their blue luminosity. Verdes-Montenegro et al. (2001) used single-dish data for 72 HCGs to examine their overall HI contents. In addition, they used high-resolution VLA mapping for 16 of these groups to investigate their H I spatial distributions and kinematics in more details. They found that, on average, HCGs contain only 40% of the expected H I mass based on the optical luminosity and morphological types of the member galaxies. Although the more deficient groups showed higher X-ray detection rate than the less deficient ones, suggesting the importance of phase transformation for the missing H I, the results were not statistically significant; subsequent analysis showed no significant correlation between H I deficiency and X-ray emission (Rasmussen et al. 2008). Verdes-Montenegro et al. (2001) also found that the individual member galaxies have higher deficiency than the group as a whole, indicating the importance

of gas removal processes from galaxies in HCGs. High angular resolution VLA observations showed that 70% of the spiral galaxies had disturbed morphology and kinematics. However, they did not find a one-to-one correlation between the amount of H I mass in tidal features and H I deficiency. This may indicate a rapid evolutionary sequence once the gas is dislodged from the member galaxies. Our data will be crucial in investigating this scenario.

Our paper is motivated by the GBT observations of Borthakur et al. (2010) and the VLA-based analysis of Jones et al. (2023). Borthakur et al. (2010) observed the H I spectrum of 26 galaxies, in which only one group was undetected. They detected diffuse H I emission, spread over  $1000 \text{ km s}^{-1}$ , which was missed by previous observations. They quantified the newly observed H I emission in terms of excess mass, which was defined as the difference between the mass measured by the GBT and the mass measured by the VLA ( $M_{\text{excess}} = M_{\text{GBT}} - M_{\text{VLA}}$ ). The excess gas mass fraction ( $M_{\text{excess}} = M_{\text{GBT}} - M_{\text{VLA}}/M_{\text{GBT}}$ ) was found to vary between 5% to 80%, and higher for more H I deficient groups. The result suggested that at least part of the missing H I was in the form of a faint, diffuse H I component, spread over a large velocity range. Despite the detection of the diffuse component, there is still a significant discrepancy between the observed H I mass and the expected values. Thus, the question of where the remaining H I in HCGs is located remains unanswered.

If the rest of the gas in HCGs is heated, we would expect to detect hot intra-group X-ray gas in H I deficient groups. However, previous observations showed that either most of the detected X-ray gas was confined within the individual member galaxies (Hess et al. 2017) or the properties of the detected hot intra-group gas among the studied H I deficient sample were very diverse and not correlated with the H I properties (Rasmussen et al. 2008). In addition, being H I deficient did not necessarily imply the presence of hot intergalactic medium (IGM) gas. For example, HCG 30 is one of the most H I deficient group, yet no hot IGM has been observed (Rasmussen et al. 2008). Previous observations also ruled out thermal evaporation as the likely dominant mechanisms to remove H I gas in HCGs (Rasmussen et al. 2008). As suggested by Hess et al. (2017), the missing H I is either too diffuse to be detected or has been ionised and is in the form of a diffuse X-ray gas that is also undetected. The increased sensitivity of new radio telescopes is promising in detecting diffuse H I component that might have been missed by previous instruments like the VLA or the Westerbork Synthesis Radio Telescope (WSRT). For example, using the Five hundred meter Aperture Spherical Telescope (FAST), Wang et al. (2023) detected faint, extended, diffuse H I emission around the tidally interacting NGC 4631 group that was missed by the WSRT. The column density of the diffuse H I was still above the critical column density for photo-ionisation and thermal evaporation. By combining data from the Karoo Array Telescope (KAT-7), WSRT, and The Arecibo Legacy Fast ALFA (ALFALFA) survey, Hess et al. (2017) also detected faint H I emission in HCG 44, far from the group centre. Thus, we expect that part of the missing H I in HCGs is in the form of extended, diffuse H I that was missed by previous observations.

In an effort to recover the missing H I in HCGs and understand more about the survival of H I in groups, we observed 6 HCGs at intermediate and advanced evolutionary stages with MeerKAT. The main scientific goals of the proposal were to:

- a) understand the transition of HCGs from a complex of H I tidal structures to the most extreme phase, where galaxies seem to have entirely lost their H I,
- b) determine the distance from the core at which the H I can survive in groups, and assess if magnetic fields aid in this survival within the harsh Intra-group Medium (IGrM),
- c) examine the effects of potential encounters with intruder galaxies located outside the field of view of the VLA,
- d) investigate the previously unexplored role of intra-group gas in the accelerated transition of galaxies from an active to quiescent state.

This paper describes the processing and general description of the data; specific goals as listed above will be addressed in future papers. This paper is organised as follows. We introduce the individual groups in section 2. We describe the observations and data reduction in section 3. We present the results in section 4. We summarise the findings and give conclusion in section 5.

**Reproducibility:** This paper is fully reproducible. We used the Snakemake workflow management system Mölder et al. (2021) to organise our scripts in terms of "rules" that contain the names of inputs and shell commands to produce different data products, figures, and tables. A single command was then used to execute the different rules sequentially and produce the final PDF paper. Snakemake is an advanced workflow management system to facilitate reproducibility and encourage transparency in scientific research by automating the execution of complex data analysis steps. This aligns with the FAIR principles (Findable, Accessible, Interoperable, and Reusable) and Open Science policies.

## 2. Sample

To have a coherent view of the evolutionary sequence of H I in HCGs, we have observed 6 HCGs, in which 3 are in phase 2 and 3 are in phase 3. We have omitted groups in phase 1 due to their similarities with galaxies in isolation. We have selected phase 2 groups since the mechanisms responsible for gas removal, dispersion or depletion are mostly active during this evolutionary stage. In addition, we have included phase 3 groups as they represent the most advanced stage of evolution, allowing us to investigate the ultimate fate of the H I gas. We list the properties of the groups in Table 1 and summarise previous findings below.

### 2.1. HCG 16

The H I spectrum of HCG 16 was obtained by Borthakur et al. (2010) using the GBT. Besides, HCG 16 was previously mapped in H I with the VLA using the C and D array configurations (Verdes-Montenegro et al. 2001; Jones et al. 2019). Jones et al. (2019) found a total mass of  $\log M_{\text{HI}}/M_{\odot} = 10.53 \pm 0.05$ . This mass is higher than the mass measured by the GBT since a significant fraction of the H I in HCG 16 was beyond the reach of the GBT field of view, which was centred at the core of the group. However, by weighting the VLA map with the GBT beam response, the measured H I mass obtained by the GBT is about 5% higher than that of the VLA (Borthakur et al. 2010). Verdes-Montenegro et al. (2001) found that most of the H I in HCG 16 was in the form of extended features such as tidal tails and bridges (see also Jones et al. 2019). The group members are connected by tidal features. The most notable one is the long tidal tail with a projected extent of 160 kpc, stretching south-east toward NGC 848 from the core of the group. Additionally, an H I

tail was found extending from HCG 16c to a faint optical counterpart located north of HCG 16a (Jones et al. 2019; Román et al. 2021). HCG 16 was also observed in H $\alpha$  and R-band by the Survey for Ionisation in Neutral Gas Galaxies (SINGG, Meurer et al. 2006). The observations revealed that all four members of HCG 16 had prominent high surface brightness (HSB) nuclear H $\alpha$  emission, with at least three members having minor-axis outflow. The deep *Chandra* X-ray and VLA-GMRT 1.4 GHz radio continuum study of O'Sullivan et al. (2014) uncovered the presence of a ridge of diffuse X-ray emission linking the four member galaxies. Their map also showed similarities between the hot and cold gas structures, with the diffuse X-ray ridge generally overlapping with the H I filaments, especially the brighter ridge connecting NGC 838 and NGC 839. However, the X-ray ridge connecting NGC 838 and NGC 835 did not match well with the H I filaments. O'Sullivan et al. (2014) detected H I X-ray, and radio continuum emission from the same region, indicating the presence of a multi-phase IGM in HCG 16.

### 2.2. HCG 30

Previous VLA observations of HCG 30 failed to detect H I in the core of HCG 30 (Jones et al. 2023). However, the GBT spectrum of Borthakur et al. (2010) showed faint, broad H I emission, spread over the whole velocity range of the group, suggesting the presence of a diffuse H I component in the group. By comparing the VLA flux with that of the GBT, Borthakur et al. (2010) found an excess gas mass fraction of 23%, corresponding to an H I excess mass of  $1.45 \times 10^8 M_{\odot}$ . Despite being the most H I deficient group (Verdes-Montenegro et al. 2001), the *Chandra* X-ray observations of Rasmussen et al. (2008) found no clear evidence of the presence of diffuse IGM emission. Various tests, including an examination of emission across their S2 and S3 CCDs and a search for radial gradients in emission did not reveal significant variation or clear spatial variations in diffuse emission. This indicated a consistency with the local background. In addition, previous observations failed to detect radio continuum emission in the group, and little far infrared emission (FIR) was observed in the member galaxies (Verdes-Montenegro et al. 2007). The group members also have little H $\alpha$  emission (Vílchez & Iglesias-Páramo 1998). Small amounts of H $\alpha$  emission were seen in the central region of the barred early-type spiral galaxy HCG 30a and HCG 30c. However, the emission in HCG 30a was contaminated by a nearby bright star, leading to a large error in the measured H $\alpha$  emission. The H $\alpha$  emission in the barred late-type spiral galaxy HCG 30b was found in its bulge. No H $\alpha$  emission was found in HCG 30d, a lenticular galaxy. Lastly, HCG 30 may have consumed all its molecular gas through star formation as evidenced by the lack of CO detection (Verdes-Montenegro et al. 1998).

### 2.3. HCG 31

HCG 31 is one of the most studied compact groups in the literature due to the peculiar characteristics of its members, such as the presence of tidal tails, a merger, and prominent starbursts. All members of HCG 31 were previously detected in H I. Their H I content range from 10% to 80% of the expected values (Verdes-Montenegro et al. 2005). However, the group as a whole is not deficient in H I. The H I observations by Verdes-Montenegro et al. (2005) revealed many tidal features, containing 60% of the total HI mass in HCG 31. In addition, all member galaxies showed signs of interactions. The H I analysis by Jones et al. (2023) using

Table 1: Group parameters

HCG	RA	Dec	Distance [Mpc]	Phase	$cz$ [km s <sup>-1</sup> ]	members	Morphology	H I content
16	02:09:31.3	-10:09:30	49	2	3957	HCG16a	SBab	Deficient
						HCG16b	Sab	Deficient
						HCG16c	Im	Normal
						HCG16d	Im	Normal
						NGC 848	Im	Normal
31	05:01:38.3	-04:15:25	53	2	4039	HCG31a	Sdm	Normal
						HCG31b	Sm	Normal
						HCG31c	Im	Deficient
						HCG31g	cI	Normal
						HCG31q	cI	Normal
91	22:09:10.4	-27:47:45	92	2	7135	HCG91a	SBc	Deficient
						HCG91b	Sc	Normal
						HCG91c	Sc	Normal
						HCG91d	SB0	No H I
30	04:36:28.6	-02:49:56	61	3	4617	HCG30a	SB	No H I
						HCG30b	Sa	No H I
						HCG30c	SBbc	No H I
						HCG30d	S0	No H I
90	22:02:05.6	-31:58:00	33	3	2638	HCG90a	Sa	Deficient
						HCG90b	E0	No H I
						HCG90c	E0	No H I
						HCG90d	Im	No H I
97	23:47:22.9	-02:19:34	85	3	6535	HCG97a	E5	No H I
						HCG97b	Sc	Deficient
						HCG97c	Sa	No H I
						HCG97d	E1	No H I
						HCG97e	S0a	No H I

**Notes.** Columns: (1) HCG ID number, (2) right ascension, (3) declination, (4) distance calculated by Jones et al. (2023), (5) the evolutionary phase of the group as originally proposed by Verdes-Montenegro et al. (2001), (6) redshift (Hickson et al. 1992), (7) core members of the group, (8) morphological types from the table compiled by Jones et al. (2023), most of which were taken from Hickson et al. (1989), (9) H I content based on the analysis of VLA archival data by Jones et al. (2023); the deficiency for each group was estimated based on the logarithmic difference between the predicted H I mass from a B-band luminosity scaling relation ( $L_B - M_{HI}$ ) of isolated galaxies and the observed H I mass.

VLA data indicated that most of the H I in HCG 31 was found in the IGrM, although no reliable separation of galaxies and tidal features was possible. Several members of HCG 31, namely E, F, H, and R, were considered to be TDGs, tidal dwarf candidates, or tidal debris (Richer et al. 2003; López-Sánchez et al. 2004; Mendes de Oliveira et al. 2006; Gómez-Espinoza et al. 2023). Despite the abundance of strong dynamical processes in HCG 31, only weak diffuse X-ray emission was detected in the group (Desjardins et al. 2013). The CO emission in HCG 31 is also faint, with enhanced CO emission found in the overlap region between HCG 31a and HCG 31c (Yun et al. 1997). This deficiency in CO was mainly attributed to tidal disruption in the group, rather than a consequence of low metal abundance.

#### 2.4. HCG 90

HCG 90 was previously imaged in H I by the ATCA and VLA, with only NGC 7172 detected (Oosterloo & Iovino 1997; Jones et al. 2023), while weak H I emission in NGC 7176 was indicated by the GBT spectrum (Borthakur et al. 2010). However, all four

members were detected in CO (Heckman et al. 1989; Huchtmeier & Tammann 1992; Verdes-Montenegro et al. 1997). CCD images taken with the 3.5 m New Technology Telescope at the European Southern Observatory (ESO) by White et al. (2003) showed that the three core members of HCG 90 are embedded in large diffuse optical light with surprisingly a very small amount of associated hot intra-cluster gas. The presence of the diffuse optical light was attributed to tidally stripped stars due to galaxy interactions. The amount of diffuse light in HCG 90 is unprecedented in comparison to either other observations or theoretical expectations involving multiple interacting systems. It has a narrow range of colour, consistent with an old stellar population. Miah et al. (2015) suggested that the diffuse light existed before the onset of the merger event in HCG 90. The *Chandra* map by Desjardins et al. (2013) showed bridges of diffuse X-ray emission connecting the three core members, as well as small common envelopes encompassing them. However, no diffuse X-ray emission associated with the IGM was found.

## 2.5. HCG 91

HCG 91 is heavily discussed in the literature due to the anomalous morphologies and kinematics of its members, including the presence of extended tidal tails, bridges, clumps, a double gaseous component, disturbed velocity field, and asymmetric rotation curves (Barnes & Webster 2001; Amram et al. 2003; Mendes de Oliveira et al. 2003; Vogt et al. 2015, 2016). The most pronounced tidal feature is the extended tidal tail of the Seyfert 1 galaxy, HCG 91a, pointing toward HCG 91c, and is visible both at optical (Eigenthaler et al. 2015) and radio wavelength (Amram et al. 2003; Vogt et al. 2016; Jones et al. 2023). Apart from HCG 91d, all other core members of HCG 91 have been detected previously in H I. The VLA maps by Jones et al. (2023) showed prominent H I tail extending to the east and curving north toward HCG 91c. In addition, HCG 91b and HCG 91c are connected by a weak extended H I emission. Overall, the VLA data showed that HCG 91 was moderately deficient in H I, containing 63% of the expected amount. At the time of writing, we are not aware of any diffuse X-ray emission measurement reported in the literature for this group.

## 2.6. HCG 97

Out of the five core members of HCG 97, only the approaching side of HCG 97b (IC5 359) was previously detected in H I in the VLA map of Jones et al. (2023), with the receding side having too low a signal-to-noise (S/N) to be included as real emission. Jones et al. (2023) suggested that HCG 97b has a disturbed morphology. This is in agreement with the LOFAR 144 MHz and VLA (1.4 GHz and 4.86 GHz) maps of Hu et al. (2023). They found a radio tail and an extended tail at the western side of HCG 97b. The radio contours are compressed at the southeastern side of the galaxy, suggesting ram-pressure stripping effects. Hu et al. (2023) used the 12m Atacama Large Millimeter Array (ALMA) and the 7m Atacama Compact Array (ACA) to trace molecular gas in HCG 97b. They detected CO emission in the disk of HCG 97 b, but not in the tails. The CO emission shows asymmetric morphology, with the southeast part showing an ‘up-turn’, consistent with the optical morphology of the disk. Diffuse X-ray emission was previously detected in HCG 97 but without any associated diffuse optical light, optical tidal features or any other (optical) signs of interactions (Pildis et al. 1995). However, the outer stellar population of HCG 97a were found to be bluer than what was expected from an elliptical galaxy. In addition, its colour was consistent with the outer envelope of HCG 97d, suggesting a previous exchange of stars between the two galaxies.

## 3. Observations and data reduction

The data was taken between July 31, 2021, and January 02, 2022, using the full MeerKAT array and a minimum of 61 antennas (proposal id: MKT-20101). The L-band receiver (856-1711.974 MHz) was used in its 32k correlator mode. The observations were centred at 1389.1322 MHz and a channel width of 26.123 KHz (or  $5.5 \text{ km s}^{-1}$  at 1420.4 MHz) was used to divide the 856 MHz total bandwidth, resulting 32768 channels. The data was recorded with the four linear polarisation products of the MeerKAT antenna feeds (XX, XY, YX, and YY). For each observing run, the primary calibrator was observed for ~8 minutes at the beginning. This was followed by a cycle of alternating observations between the gain calibrator (~2 minutes) and the target (~38 minutes), with the primary calibrator revisited every two hours. Polarisation calibrators were observed twice for ~6

minutes. The total time spent per group was ~6.25 hours (about 5.13 hours spent on source) or a total of 37.5 hours, including calibration overheads, at 8 seconds integration period for the six HCGs. Table 2 shows the calibrators used and the observing time spent on each target.

The raw data were processed using the CARACal pipeline (Józsa et al. 2020). CARACal integrates various radio astronomical software that can be executed through a Stimela script (Makhathini 2018), enabling a user control over each step of the data processing. To produce a science-ready H I data cube, the raw data were passed through three main steps, called workers, in CARACal:

1. flagging and cross-calibration,
2. continuum imaging and self-calibration,
3. continuum subtraction and line imaging.

CARACal produces various diagnostic plots that can be visually inspected to assess the quality of the data products. Our data was processed on a virtual machine of the Spanish Prototype of the Square Kilometre Array (SKA) Regional Center (espSRC, Garrido et al. 2022). The virtual machine has 24 CPUs and 186 GB RAM. The espSRC is hosted by the Institute of Astrophysics of Andalusia (IAA-CSIC). It serves as a test bed for future scientific activities with the SKA while promoting Open Science and FAIR principles. We adopt a similar data reduction strategy as described by Serra et al. (2023). However, our observations consist of a single pointing rather than a mosaic. We describe our data reduction process below.

### 3.1. Flagging and cross-calibration

Briefly, flagging and cross-calibration were first applied to the calibrators before performing on-the-fly calibration and flagging on the target. The detailed steps are as follows. First, auto-correlations and shadowed antennas were flagged using the Common Astronomy Software Applications (CASA) task `flagdata` incorporated in CARACal. RFI was then flagged using `AOFlogger` (Offringa et al. 2012), which is the default option in CARACal. Next, cross-calibration was performed. For the primary calibrator, time-dependent delay calibration ( $K$ ) was first carried out, followed by gain calibration ( $G$ ) while applying the derived  $K$  term on the fly. After that, bandpass calibration ( $B$ ) was run while applying the previous  $K$  and  $G$  terms on the fly. This sequence was repeated twice (order: KGBKGB in CARACal) before applying the primary calibrator delay and bandpass to the secondary calibrator (apply: KB in CARACal) and solving for gain amplitude and phase. Next, flagging was performed to remove spurious calibrated visibilities before solving again for the gain amplitude and phase, and additionally bootstrapping the flux scale from the primary calibrator (order: GAF and `calmode: [ap, null, ap]` in CARACal). For the target, on-the-fly calibration, applying the primary calibrator delays and bandpass, as well as the secondary calibrator gains, was carried out. Auto-correlations, shadowed antennas, and RFI were also flagged.

### 3.2. Continuum imaging and self-calibration

This step is part of the `selfcal` worker in CARACal to get continuum models and perform self-calibration. High signal-to-noise (S/N) continuum images and polarisation data will be described in a future paper. Here, we only describe steps relevant for H I line imaging. We use `WSClean` (Offringa et al. 2014) for imaging and `Cubical` (Kenyon et al. 2018) for self-calibration.

Table 2: Observational properties

HCG	Observing time		Flux cal.	Gain cal.	Polarisation cal.	Antennas
	Total	On source				
16	6.27	5.14	J0408-6545	J0240-2309	J0521+1638	61
31	6.21	5.15	J0408-6545	J0503+0203	J0521+1638	62
91	6.26	5.14	J1939-6342	J2206-1835	J0137+3309 J0521+1638	61
30	6.21	5.15	J0408-6545	J0423-0120	J0521+1638	62
90	6.27	5.15	J1939-6342	J2214-3835	J0137+3309 J0521+1638	63
97	6.26	5.15	J1939-6342 J0408-6545	J0022+0014	J0521+1638 J0137+3309	63

**Notes.** Columns: (1) HCG ID number, (2) total and on-source observing time in hours, (3) flux calibrators, (4) gain calibrators, (5) polarisation calibrators, (6) number of available MeerKAT antennas at the time of observations.

Radio continuum emission was iteratively imaged and self-calibrated. At each step, WSClean was allowed to clean blindly down to a masking threshold set by us. At each new iteration, the previous clean mask was used to allow for a deeper cleaning. Multi-scale cleaning was used, with scales automatically selected by the algorithm. WSClean was run on a  $2 \text{ deg} \times 2 \text{ deg}$  image with  $1''$  pixel size using Briggs weighting of -1 with  $0''$  tapering. Three calibration iteration was used, requiring four WSClean imaging with different clean mask threshold (auto-mask option for WSClean): 30, 20, 10, and 5 times the rms noise level. The same cleaning threshold, 0.5 (auto-threshold parameter for WSClean), was used for each imaging option.

### 3.3. Continuum subtraction and line imaging

The continuum model generated in the previous step was subtracted from the target visibilities. Additionally, doppler-tracking corrections and a first-order polynomial fitting to the real and imaginary parts of the line-free channels were carried out with the CASA task `mstransform` in CARACal. Next, any erroneous visibilities produced by `mstransform` were flagged with `AOflogger` (Serra et al. 2023). After that, H I data cubes were produced with WSClean using different imaging parameters. Multi-scale cleaning was used using a major cycle clean gain of 0.2 and scales were automatically selected by WSClean. For each group, we made available cubes at  $60''$ , as well as higher resolution cubes down to  $20 \text{ kpc}$  linear resolution, roughly corresponding to the scale length of the optical disk. Cubes at intermediate resolutions are also available. The  $60''$  cubes allow the study of extended emission; whereas the higher resolution cubes aid at separating galaxies from tidal tails or intra-group gas as previously done by Jones et al. (2023). To get the final data cubes for each group, we run CARACal to obtain a cube at  $98''$ . Then, we run the Source Finding Application (SoFiA, Serra et al. 2015; Westmeier et al. 2021) outside of CARACal to get a better clean mask. After that, we run CARACal again using that mask to get our final lowest-resolution data cube. We again use SoFiA outside of CARACal to get another clean mask and use it to clean the next higher-resolution cube. We proceed like this until the highest resolution cube. To correct for primary beam attenuation, we used the model of Mauch et al. (2020). To convert the cubes from frequency to velocity, we used the MIRIAD task `VELSW`. Throughout this paper, we use the optical velocity definition. We also use the  $60''$  cube unless stated otherwise.

## 4. Results

The basic data products consist of data cubes, moment maps, and integrated spectra for the group as a whole, as well as source catalogues, cubelettes, moment maps, position velocity cuts, integrated spectra for each source detected by SoFiA, and 3D visualisation of each group. We used ViSL3D (Labadie-García et al. 2024), a new 3D visualisation software built upon X3D pathway (Vogt et al. 2016) to construct the 3D view of each cube, which can be used to facilitate the separation of different H I structures based on spatial and kinematical information. They are available at <https://amiga.iaa.csic.es/x3d-menu/>. For each of the groups, we provide two versions of the data cube: one showing the large-scale structures and one highlighting the central part of the group. The user can toggle between different iso-surface levels to make it easier to identify low-column density features. The technical details underlying their construction will be described in Labadie et al. (in prep.) A thorough 3D analysis of the different H I features in HCGs is beyond the scope of this paper. Figure 1 shows examples of data products for NGC 1622 at  $43.8'' \times 47.5''$  resolution, a spiral galaxy previously detected in H I located at about  $381 \text{ kpc}$  south east from the group centre. Below we describe the data for the individual groups. Overall, we observed even more extended tidal features in phase 2 groups than previously reported. For phase 3 groups, we did not detect any diffuse H I component, though we did identify some new high surface brightness features. Numerous galaxies were detected around the group centres, most notably in HCG 97 and HCG 91, suggesting that these groups may be embedded within larger structures. Additionally, some of the detected galaxies lack optical counterparts.

### 4.1. GBT vs MeerKAT flux

To compare our flux measurements with the single dish GBT ones by Borthakur et al. (2010), we followed the procedures outlined in that paper. They used the AIPS task `PATGN` to model the GBT beam response as a two-dimensional Gaussian with a FWHM of  $9'.1$  defined by:

$$f(R) = C3 + (C4 - C3) \exp[-((0.707/C5)^2 R^2)], \quad (1)$$

where  $R$  is the radius,  $C3$  is the minimum response of the beam, which is equal to zero,  $C4$  is the maximum response of the beam, which is equal to 1, and  $C5$  is the width of the distribution in arc second, which in our case, is equal to  $9.1 \times 60 / 2.355$ . The output

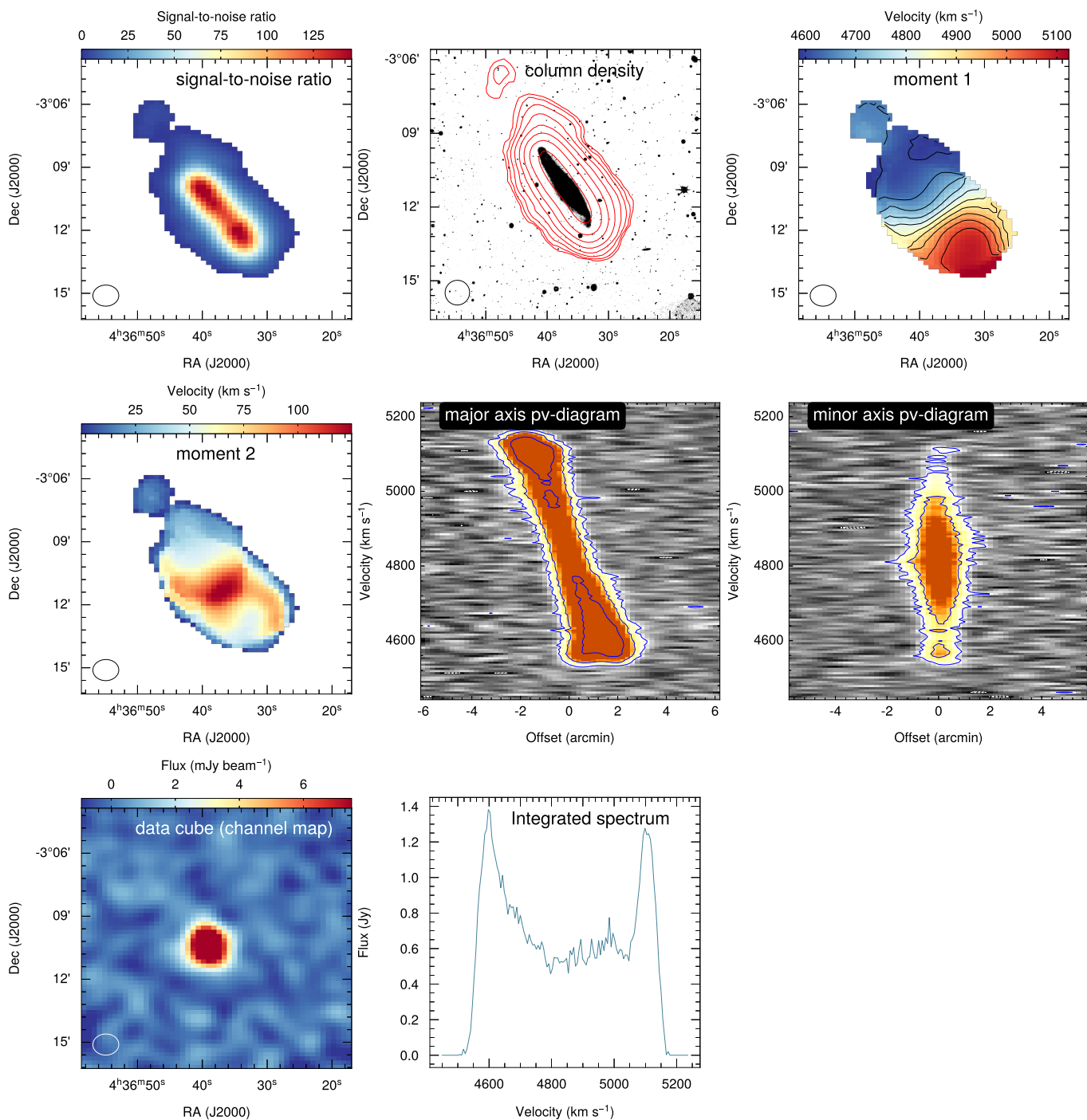


Fig. 1: Example SoFiA data products for NGC 1622, a spiral galaxy previously detected in H I located at about 381 kpc south east from the group centre. From top left to bottom right panel: signal-to-noise ratio of each individual pixels, column density map and R-band DeCaLS DR10 (Dey et al. 2019) optical image — the contour levels are  $(5.70 \times 10^{18}, 1.140 \times 10^{19}, 2.28 \times 10^{19}, 4.56 \times 10^{19}, 9.12 \times 10^{19}, 1.82 \times 10^{20}, 3.65 \times 10^{20}, 7.30 \times 10^{20}) \text{ cm}^{-2}$ , first moment map (velocity field), second moment map, major axis position velocity diagram, minor axis position velocity diagram, an example channel map, and integrated spectrum from a data cube where the noise has been masked. The ellipse at the bottom left corner of each plot shows the beam,  $43.8'' \times 47.5''$ .

of PATGN is a two-dimensional map containing the GBT beam correction factor. For the sake of reproducibility, we wrote a python function to generate the GBT beam response using equation 1. We multiply it with every channel of the MeerKAT cube. Then, we derived the integrated spectrum from the full area of the resulting cube. Our procedure ensures that emission outside the primary beam of the GBT is tapered to allow a reasonable

comparison with the MeerKAT spectrum. We used the original, unsmoothed spectrum of Borthakur et al. (2010) and divided the observed brightness temperature by the antenna gain correction factor, 1.65 K/Jy, measured by the authors to convert it to Jy. We compare the GBT and MeerKAT integrated spectra in Figure 2. For a better visualisation, we have smoothed the spectra from both telescopes to a common velocity resolution of  $20 \text{ km s}^{-1}$  us-

ing a boxcar kernel. For phase 2 groups, the agreement is good, the MeerKAT and GBT spectra agree well with each other in terms of shape and recovered flux. For phase 3 groups, the agreement is less obvious. For HCG 30, MeerKAT recovers less emission around the velocities of HCG30b, HCG30c, and HCG30d. For HCG 90, the GBT and MeerKAT spectra seem to agree with each other except around  $3500 \text{ km s}^{-1}$  where the GBT spectrum shows positive emission. For HCG 97, the GBT spectrum shows emission spreading across a large velocity range. However, that of MeerKAT shows narrower emission. In addition, at virtually each velocity of HCG 97, GBT recovers more flux than MeerKAT. Figure 3 and Table 3 compares the flux measured by MeerKAT and GBT within the GBT beam area. For phase 2 groups, there is a good agreement between the flux recovered by the GBT and MeerKAT within this area, with the largest flux difference being 22%. For the groups in phase 3, GBT recovers over 70% more flux than MeerKAT for HCG 30 and HCG 97, while for HCG 90, MeerKAT recovers 32% more flux than GBT. This is partly due to the presence of negative fluxes in the GBT spectrum of HCG 90. Additionally, the MeerKAT spectrum around the velocity of HCG 90a peaks well above that of the GBT. Note that the total flux recovered by MeerKAT is significantly higher than that of the GBT due to the much larger field of view of MeerKAT. We summarise the observational parameters and derived H I mass for each group in Table 4 and compare them with the corresponding VLA data from Jones et al. (2023). To calculate the noise level listed in the table, we use the noise cubes generated by SoFiA. First, we take the median value of each velocity slice across the noise cube. Then we take the median of the values from the slices. Note that the noise has been estimated using the non-primary beam corrected data. However, the tabulated mass is calculated from the global profile of the primary beam corrected cubes using the following formula:

$$M_{\text{HI}}[M_{\odot}] = 235600 \times D^2 \times \sum S_i \Delta v \quad (2)$$

where  $\sum S_i \Delta v$  is the sum of the flux over all channels and within the field of view of MeerKAT in units of  $\text{Jy km s}^{-1}$ , and  $D$  is the distance to the group. As described by Serra et al. (2023), excluding channels containing known H I line emission while performing continuum subtraction using the UVLIN option of the CASA task `mstransform`, implemented in CARACaL, can introduce artefacts in the form of vertical stripes in a RA-velocity slice from the data cube. To check the possible presence of RFI or continuum residual emission in channels excluded from the visibility fit, we show a plot of the RA-velocity slice at the central declination of each HCGs cube. We describe the data products for each group below.

#### 4.2. HCG 16

We show the RA-velocity slice of HCG 16 in the first panel of Figure 4. We found no obvious RFI or continuum residuals. We plot the median noise level of the data cube as a function of velocity in the second panel of the figure. The noise does not change much across the spectral channel. We plot the integrated spectrum of the group in the right panel of Figure 4. The spectrum was derived from the primary beam corrected cube where the noise was blanked using a 3D mask generated by SoFiA. The most significant discrepancies between the VLA and MeerKAT spectra are observed at the velocities corresponding to galaxies HCG 16c and HCG 16d. Note that HCG 16c is the the group's most active star-forming galaxy and is strongly interacting with HCG 16d (Jones et al. 2023). The difference between the VLA

Table 3: GBT vs MeerKAT recovered H I flux

HCG	MeerKAT [Jy km s <sup>-1</sup> ]	GBT [Jy km s <sup>-1</sup> ]	Difference [%]
16	20.54	21.62	-5
31	22.76	25.32	-10
91	7.97	10.18	-22
30	0.16	0.56	-73
90	1.31	0.89	+32
97	0.69	3.31	-79

**Notes.** Difference in percentage between the integrated flux recovered by GBT and MeerKAT within the GBT beam area. The negative sign in the table indicates that MeerKAT recovers less flux than the GBT. The positive sign indicates that MeerKAT recovers more flux than the GBT.

and MeerKAT spectra can be attributed to MeerKAT's capability to detect more tidal features than the VLA. Although MeerKAT detected more H I features as will be explained in the next section, the total mass recovered is remarkably similar to that observed by the VLA.

We show example channel maps of the central part of HCG 16 in Figure 5. The rest is available [online](#). As also mentioned in Jones et al. (2019), the NW tail, apparent in the moment maps, is not visible in the channel maps. In contrast, the NE tail is clearly visible and appears to be dislodged gas from HCG 16c. As can be seen from the channel map at  $\sim 3966 \text{ km s}^{-1}$ , the SE tail is made of gas coming from both NGC 848 and HCG 16d, extending across about seven channels. The hook feature becomes more distinct at  $\sim 4034 \text{ km s}^{-1}$ . The channel maps clearly show the double sided tails of HCG 848, i.e., the hook-like feature and part of the gas that makes up the SE tail.

In Figure 6, we show maps of the H I sources detected by SoFiA within the MeerKAT field of view. The left panels show all sources detected by SoFiA. The right panels highlight the central part of the group. In total, SoFiA detected nine surrounding members; their properties are discussed in an accompanying paper. In the top panels of the figure, we show the column density maps of HCG 16 overplotted on top of DeCaLS R-band (Dey et al. 2019) optical images. The moment one map of the group is shown in the bottom panel of Figure 6, which is plotted in a way that each individual members are scaled by different colour-scaling factor to highlight any rotational patterns. The surrounding members show differential rotation with an apparently undisturbed H I morphology. However, the integrated iso-velocity contours of the centre of the group as a whole are disturbed. Note though that the individual members may still have their rotation. The most remarkable finding here is the presence of numerous tidal features and clumps, as well as a long, continuous tidal tail connecting the core member of the group with NGC 848. In addition, a hook-like structure extends south-east of NGC 848 before curving to the north west in direction parallel to the main group. As shown in Figure 7, all core members are linked by tails or high column density bridges. There is a continuity in velocity between NGC 848S and the curved tail. The hook appears to be a stretched gas from NGC 848 due to its encounter with the main group. The presence of numerous tails and clumps are typical of compact groups at the intermediate stage, indicating substantial gas loss into the IGM. To better visualise the tails, we show segmented position-velocity diagrams, taken from the paths shown in Figure 7, in Figure 8 as previously done by Jones et al. (2019) using VLA data. Most of the tails were



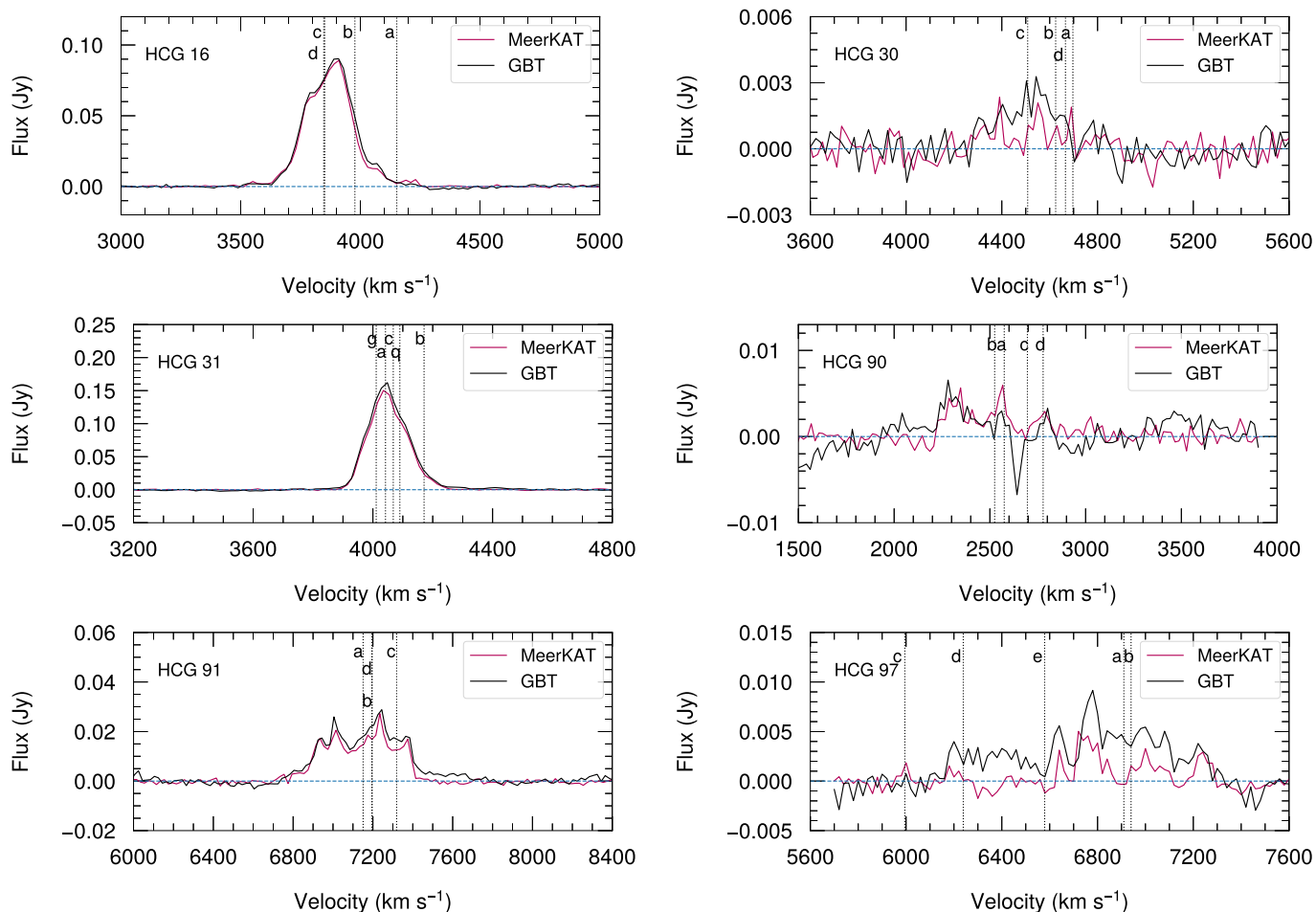


Fig. 2: GBT vs MeerKAT integrated spectrum smoothed at  $20 \text{ Jy km s}^{-1}$ . The pink solid lines indicate the MeerKAT integrated spectra. The solid black lines indicate the GBT spectra of [Borthakur et al. \(2010\)](#). The vertical dotted lines indicate the velocities of the galaxies in the core of each group. The horizontal blue lines indicate zero intensity values to guide the eyes.

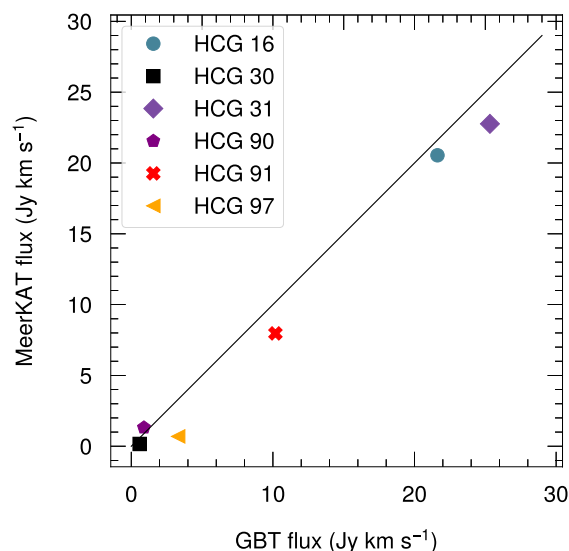


Fig. 3: GBT vs MeerKAT integrated flux measured within the GBT beam area. The solid line is a line of equality.

previously identified by the VLA map of [Jones et al. \(2019\)](#) and

we adopt the author's nomenclature to name them. However, the tails are more pronounced in the MeerKAT map. Note also that the curved tail (hook) was not visible in the VLA map.

The 3D visualisation of the group is shown in Figure 9. The left panel highlights high column density HI, whereas the right panel shows superposition of iso-surface corresponding to both low and high column density gas. This kind of visualisation is very crucial to identify features not associated with the disk of the member galaxies. The connection between all member galaxies is evident. A high surface brightness bridge connects the core of the group and NGC 848. The hook is composed of lower column density gas, stretching from NGC 848 before bending upward.

#### 4.3. HCG 31

The RA-velocity slice shown in the left panel of Figure 10 shows no apparent RFI or continuum residuals. In addition, the median noise values as a function of velocity, in the middle panel of the figure, do not change much. We compare the global spectrum of HCG 31 from the VLA with that from MeerKAT in the right panel of Figure 10. It's clear that MeerKAT recovers more HI emission than VLA at virtually all the velocity range of the group. The largest difference in terms of recovered flux corresponds to the A+C complex. Therefore, most of the new tidal

Table 4: Observational parameters and derived H I mass

HCG	Distance [Mpc]	Pixel size ["]	Weighting	$uv$ taper ["]	Beam size		Lin. res.	
					MeerKAT ["]	VLA ["]	MeerKAT [kpc]	VLA [kpc]
16	49	12	0.5	50	57.9×57.5	38.9×31.7	13.5×13.4	9.2×7.5
31	53	12	0.5	50	59.9×59.2	14.6×12.1	15.4×15.2	3.8×3.1
91	92	12	0.5	50	58.0×56.1	51.3×47.0	25.6×25.0	22.9×21.0
30	61	12	0.5	50	60.5×59.8	57.9×44.8	17.9×17.7	17.1×13.2
90	33	12	0.5	50	57.7×56.7	49.1×39.9	9.2×9.1	7.9×6.4
97	85	12	0.5	50	60.2×59.3	63.2×49.5	23.8×23.3	26.0×20.4

HCG	Noise		$N_{\text{HI}}(3\sigma)$		Flux		V. range [km s <sup>-1</sup> ]	H I mass	
	MeerKAT [mJy beam <sup>-1</sup> ]	VLA	MeerKAT [10 <sup>18</sup> cm <sup>-2</sup> ]	VLA	MeerKAT [Jy km s <sup>-1</sup> ]	VLA		MeerKAT [10 <sup>9</sup> M <sub>⊙</sub> ]	VLA
16	0.33	0.41	3.5	22.5	42.2	39.5	2811 - 5006	23.9	22.4
31	0.33	0.65	3.3	176.1	37.6	22.1	2095 - 5986	24.9	14.7
91	0.33	0.66	3.7	18.5	55.3	15.8	4015 - 10994	110.5	31.6
30	0.33	0.51	3.3	13.3	40.0	15.1	3251 - 5733	35.1	13.3
90	0.32	0.55	3.4	26.9	40.8	3.4	507 - 5010	10.5	0.9
97	0.32	0.44	3.2	9.5	17.7	7.0	5232 - 8247	30.2	11.9

**Notes.** Top: (1) HCG ID number, (2) distance derived by Jones et al. (2023), (3) Pixel size of the data cubes, (4) Briggs weighting parameters, (5) Gaussian taper, (6) the synthesised beam size, (7) Linear resolution. Bottom: (1) HCG ID number, (2) the median noise level of the data cubes, (3) the  $3\sigma$  column density sensitivity limit assuming an H I line width of 20 km s<sup>-1</sup>, (4) total H I flux, (5) Velocity range used to calculate the total H I flux (6) total H I mass. The VLA data is from Jones et al. (2023).

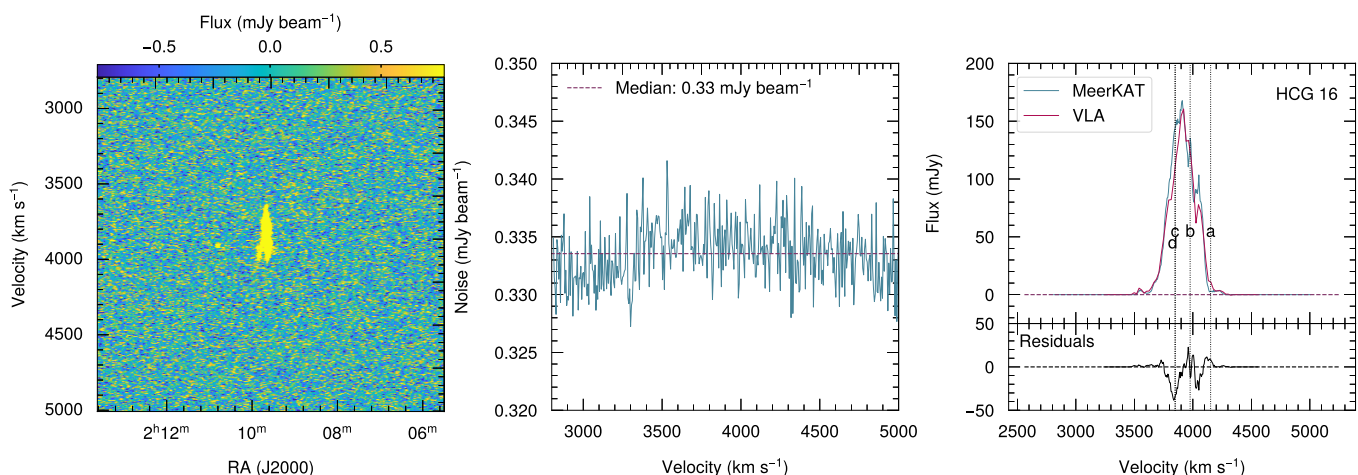


Fig. 4: Left panel: velocity vs right ascension of HCG 16. Middle panel: median noise values of each RA-DEC slice of the non-primary beam corrected 60'' data cube of HCG 16 as a function of velocity. The horizontal dashed line indicates the median of all the noise values from each slice. Right panel: the blue solid lines indicates the MeerKAT integrated spectrum of HCG 16; the red solid line indicates VLA integrated spectrum of the group derived by (Jones et al. 2023). The vertical dotted lines indicate the velocities of the galaxies in the core of the group. The spectra have been extracted from area containing only genuine H I emission.

features we detected is expected to be coming from the A+C complex. This is not surprising since HCG 31A and HCG 31C are known to be in the process of merging and their interactions are expected to produce many tidal features into the IGM. Note though that separating features in HCG 31 is extremely challenging (Verdes-Montenegro et al. 2005; Jones et al. 2023) and may require complex kinematic analysis that we will investigate in a future paper.

Example channel maps of HCG 31 are shown in Figure A.1, and the rest is available online. Visual inspections indicate that the south-eastern and the north-western elongated H I is most

likely associated with the A+C complex. Part of the northern extension could be coming from HCG 31Q, though. The elongation of the south-eastern tail is likely a result of gas being stripped away during the interaction between HCG 31A and HCG 31C, which then subsequently extended by a fly-by encounter between member G and the A+C complex. There are no known optical counterparts associated with the extended H I emission. Thus, they are not the results of interactions with members outside the central galaxies. The highest H I peak is associated with HCG 31C, which also corresponds to sites of active star forming regions.

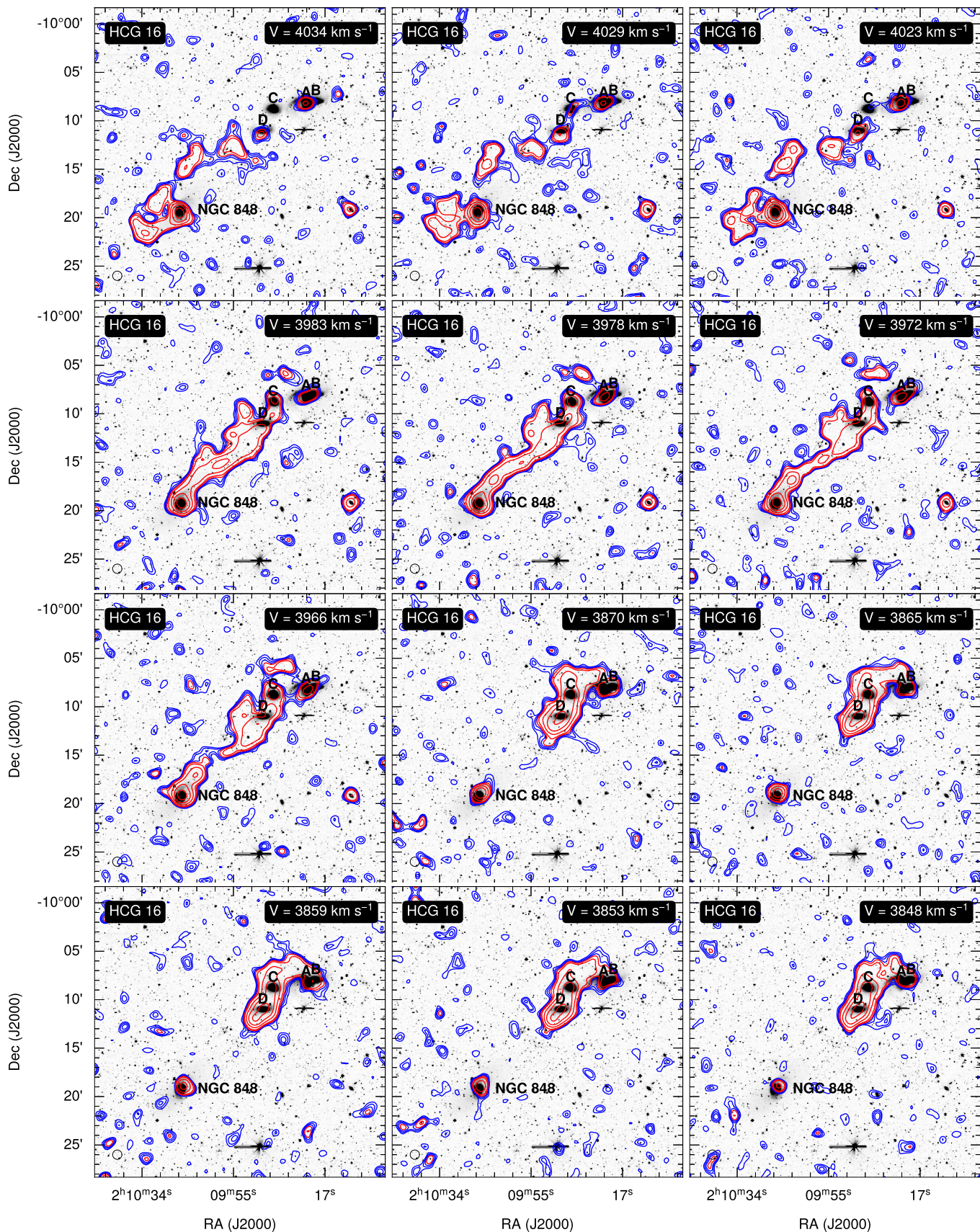


Fig. 5: Example channel maps of the primary beam corrected cube of HCG 16 overlaid on DECaLS DR10 R-band optical images. Contour levels are (1.5, 2, 2.5, 3, 4, 8, 16, 32) times the median noise level in the cube ( $0.58 \text{ mJy beam}^{-1}$ ). The blue colours show contour levels below  $3\sigma$ ; the red colours represent contour levels at  $3\sigma$ , or higher. More channel maps can be found [here](#)

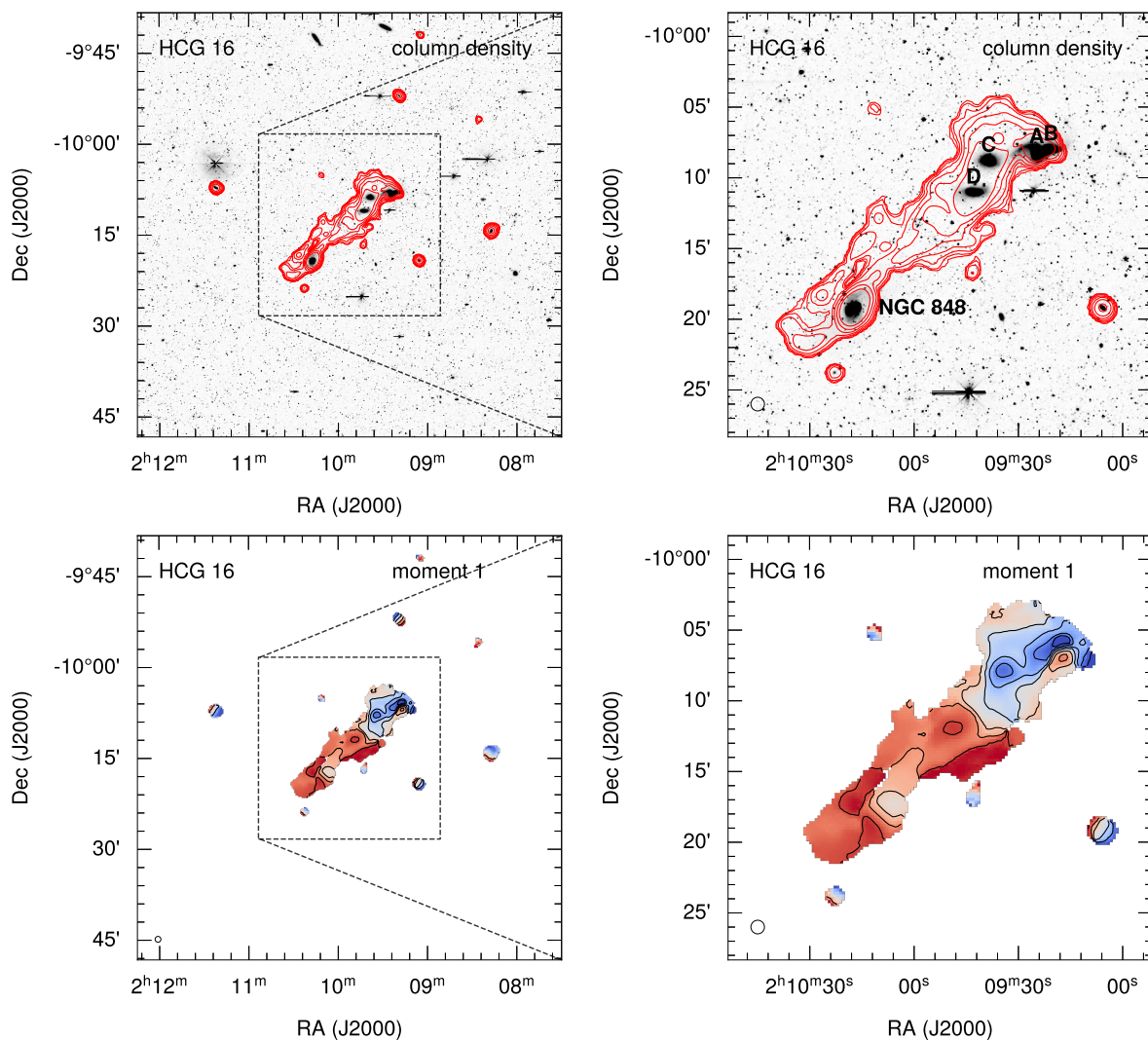


Fig. 6: H I Moment maps of HCG 16. Left panels show all sources detected by SoFiA. The right panels show sources within the rectangular box shown on the left to better show the central part of the group. The top panels show the column density maps with contour levels of ( $3.1 \times 10^{18}$ ,  $6.2 \times 10^{18}$ ,  $1.2 \times 10^{18}$ ,  $2.5 \times 10^{19}$ ,  $5.0 \times 10^{19}$ ,  $9.9 \times 10^{19}$ ,  $2.0 \times 10^{20}$ )  $\text{cm}^{-2}$ . The contours are overlaid on DECaLS DR10 R-band optical images. The bottom panels show the moment one map. Each individual source has its own colour scaling and contour levels to highlight any rotational component.

We show the moment maps of HCG 31 in Figure A.2. The central part of HCG 31 is detected as one source although it is composed of five late-type galaxies and four tidal dwarf candidates. The surrounding members seem to have differential rotation and present no obvious signs of interactions. However, the integrated iso-velocity contours of the central part of the group as a whole is clearly disturbed, although the H I disk of the individual core members may still have rotation. The H I moment map is elongated towards the south-east and the north-west, which was not visible in previous VLA maps. The DeCaLS image shows no optical counterparts within the elongated region. We show the column density map of the central part of HCG 31 from a  $15.47'' \times 11.86''$  datacube in Figure A.3. We also show the previously identified tidal fragments and tidal dwarf candidates mentioned in Mendes de Oliveira et al. (2006). The A+C complex, HCG 31B, and the tidal fragments/dwarf candidates are embedded in high column density features, with the highest contour corresponding to the overlap area between A and C and also to F1. All the tidal fragments and the tidal dwarf candidates are

embedded in a tail connecting HCG 31 G and the other core members.

We show the 3D visualisation of HCG 31 in Figure A.4. The left panel emphasises regions of high H I column density, while the right panel displays a superposition of iso-surfaces representing both low and high column density gas. Similar to HCG 16, significant tidal features are observed in the group as a result of the ongoing interactions and mergers among the member galaxies.

#### 4.4. HCG 91

The RA-velocity plot of HCG 91 is shown in the first panel of Figure B.1. There are subtle vertical stripes at velocities corresponding to channels excluded during UVLIN fit. The effects can be seen in the noise-velocity plot in the middle panel of Figure B.1 where the noise increases at the channels where known emission is excluded while performing UVLIN fit. Unfortunately, we cannot correct for such effects. This is inherent to UVLIN as

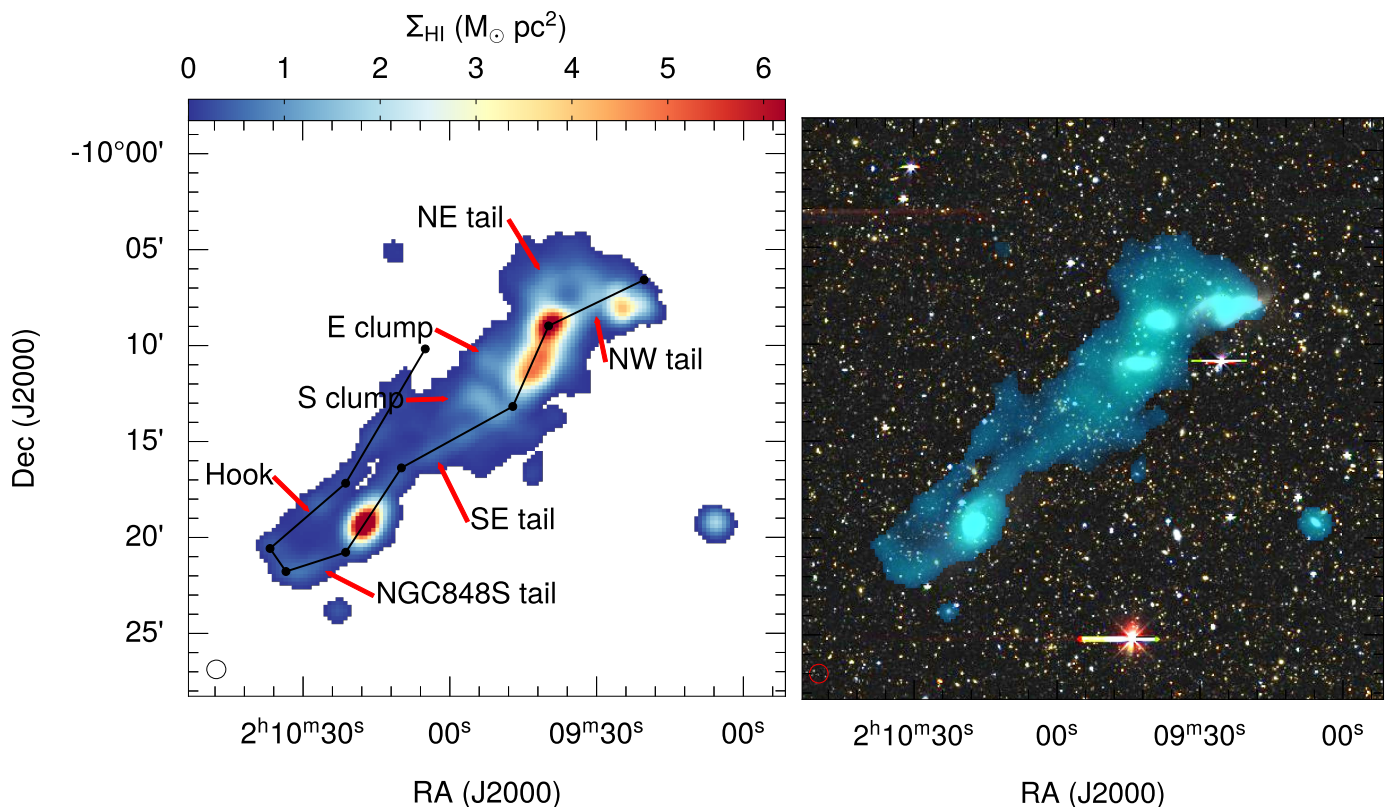


Fig. 7: Left panel: MeerKAT H I surface density map of HCG 16 showing the paths (black lines) from which the segmented position-velocity diagrams shown in Figure 8 are taken. The black circles show the positions of the nodes that make up the different slices. Right panel: The same moment zero map overlaid on DECaLS optical images to highlight the core members.

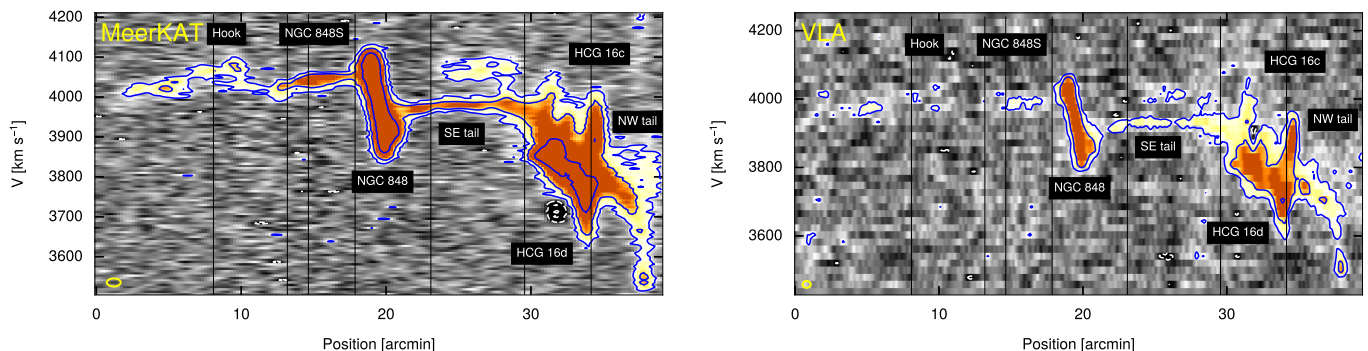


Fig. 8: Segmented position-velocity diagrams of HCG 16 taken from the paths shown in Figure 7. Left panel: MeerKAT data from this paper, right panel: VLA data from Jones et al. (2019). Blue contours show emission at  $3 \times$  the rms noise. Dashed lines show negative contours. The vertical black lines indicate the positions of the nodes that make up the slices from which the position velocity diagrams were taken. The yellow ellipses at the bottom left corner of each panels show the half-power beam width  $\sqrt{BMAJ * BMIN}$  and  $20 \text{ km s}^{-1}$  velocity width.

described in Serra et al. (2023). We show the global profiles of HCG 91 from the VLA and MeerKAT in the right panel of Figure B.1. MeerKAT detects much more H I emission than the VLA due to its larger field of view of MeerKAT and better sensitivity. As shown in the global profiles, there are many sources beyond the velocity range of the central part of the group and some or many of them might still belong to the group. A more careful study of them will be done in an accompanying paper (Sorgho et al. in prep).

We show example channel maps of HCG 91 in Figure B.2, which contain the SE tail of HCG 91a. Additional channel maps are available online. Some of the  $2\sigma$  contours of HCG 91a bend toward the north, and appear to be aligned with its optical tails. In addition, the curved H I emission that apparently connects HCG 91c and HCG 91d in projection appears as broken contours of low-column density gas coming from both HCG 91c and HCG 91b. Lastly, the channel maps show no H I emission at the velocity and location of HCG 91d. This galaxy has never been detected in H I emission before (Jones et al. 2023).

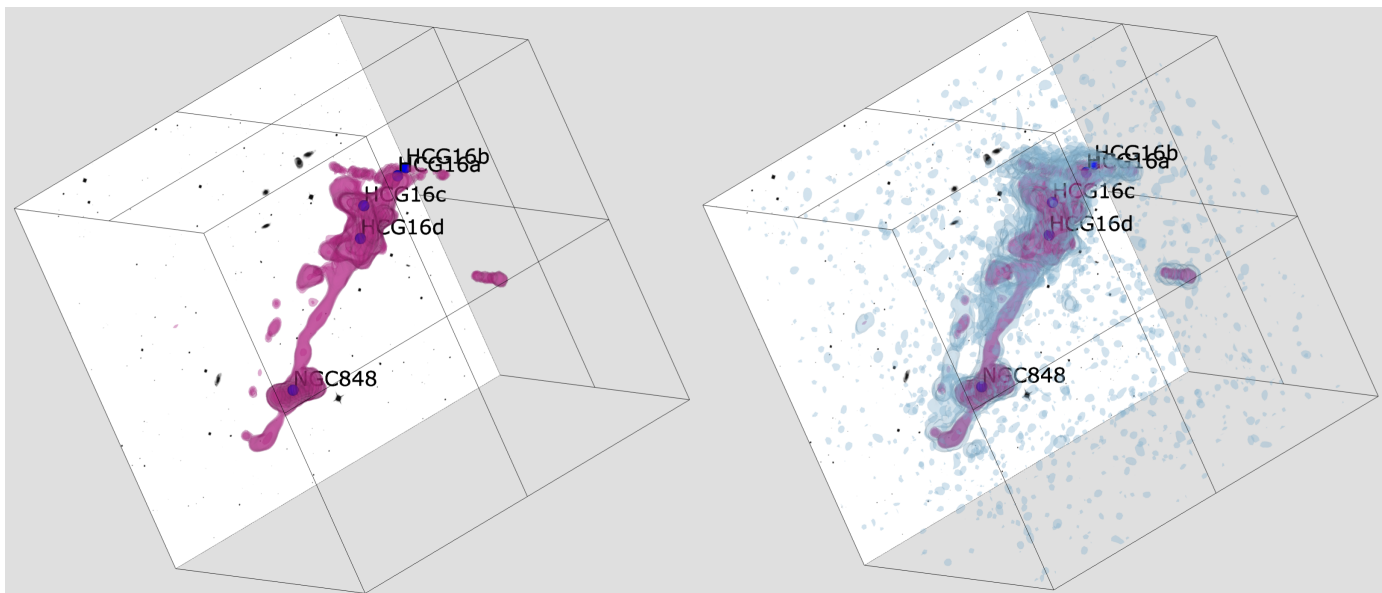


Fig. 9: 3D visualisation of HCG 16. The left panel shows iso-surface level highlighting the high-column density gas. The right panel showcases the low-column density H I gas. The 2D grayscale image is a DeCaLS R-band optical image of the group. The blue circles indicate the position of the member galaxies. The 2D grayscale image is a DeCaLS R-band optical image of the group. The online version of the cubes are available at <https://amiga.iaa.csic.es/x3d-menu/>.

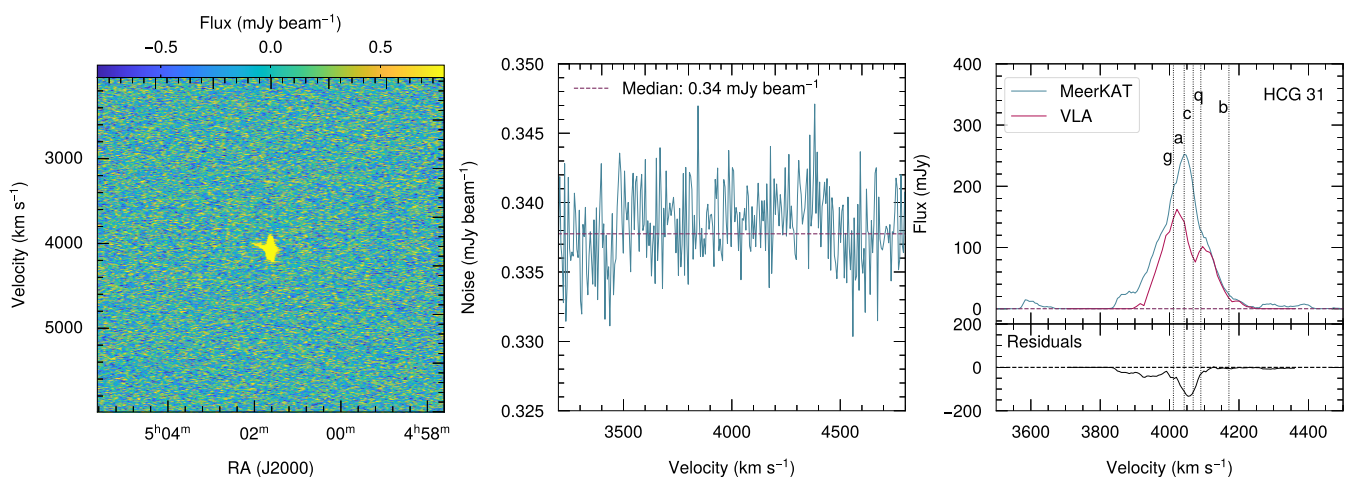


Fig. 10: Left panel: velocity vs right ascension of HCG 31. Middle panel: median noise values of each RA-DEC slice of the non-primary beam corrected 60'' data cube of HCG 31 as a function of velocity. The horizontal dashed line indicates the median of all the noise values from each slice. Right panel: the blue solid lines indicates the MeerKAT integrated spectrum of HCG 31; the red solid line indicates VLA integrated spectrum of the group derived by (Jones et al. 2023). The vertical dotted lines indicate the velocities of the galaxies in the core of the group. The spectra have been extracted from area containing only genuine H I emission.

We show the moment maps of HCG 91 in Figure B.3. We have detected many sources in HCG 91 but only those within  $1000 \text{ km s}^{-1}$  from the systemic velocity are shown here. On projection, the core members and a far-off members at the west side, LEDA 749936, are embedded in one common H I envelop. Two H I bridges connect HCG 91b and HCG 91c. The first was identified previously by Jones et al. (2023) which they separated as intra-group gas. The second one extends to the west from HCG 91c before curving toward the north to join another extended feature of HCG 91b. In addition, it seems to elongate towards LEDA 749936. Another higher S/N emission connects HCG 91c and HCG 91a. All the core members of HCG 91, including the detection slightly far west are detected as one source

by SoFiA, highlighting the complex interactions between the members. We also show the velocity fields of the galaxies in the core of HCG 91 in Figure B.4 from a data cube at  $24.0'' \times 20.2''$ , as well as their DeCaLS optical image along with their H I iso-velocity contours. Their optical major axis position angles are well aligned with their H I major axis position angles. However, the outer disk of HCG 91b is warped. HCG 91a has asymmetric double-horned profiles, typical of spiral galaxies. Its main disk still has a clear rotational pattern; however, its halo is disturbed. HCG 91c also has asymmetric double-horned profiles. In addition, its main disk has retained rotation despite the interaction with other members. The blue-shifted velocity field of HCG 91b is more or less regular, ex-

cept the warp mentioned earlier. However, the red-shifted part is clearly disturbed due to the interaction with HCG 91c. The H I emission in LEDA 749936 has very low S/N and its velocity field is disturbed. It has a single peaked global profile, typical of dwarf galaxies. We detect many sources around the central part of HCG 91 that seem to have regular rotation. However, a group of four strongly interacting galaxies can be seen south-east of the core members. Their H I velocity fields and morphologies are clearly disturbed. In addition, two interacting galaxies are found further east. Note though that their systemic velocities differ by about  $1500 \text{ km s}^{-1}$  compared to those of the core groups.

We show the 3D visualisation of HCG 91 in Figure B.5. Again, the left panel showcases regions of high H I column density, while the right panel illustrates a composite view, overlaying both low and high column density gas distributions. This group appears to be less chaotic than HCG 16 and HCG 91, and has a lot less low surface brightness features. HCG 91b and HCG 91c are connected by a hook like high surface brightness features and a low column density bridge. However, there is no H I connection between HCG 91c and HCG 91a. The overall morphology of the member galaxies are clearly disturbed, especially that of HCG 91a. It is also clear from the 3D view that no H I has been detected in HCG 91d.

#### 4.5. HCG 30

The RA-velocity plot of HCG 30 is presented in the left panel of Figure C.1, showing no apparent signs of continuum residuals or cleaning artefacts. The median noise of the data cube as a function of velocity is shown in the middle panel of the figure. The comparison of the MeerKAT and VLA global profile is shown in the right panel of Figure C.1. The larger field of view of MeerKAT and the detection of new features and a member in the central part of HCG 30 makes the global profile of MeerKAT much brighter than that of the VLA.

We present the example channel maps of HCG 30 in Figure C.2. These only show the channels corresponding to the receding side of HCG 30b, the rest is presented online. Overall, the emission is faint and is mostly below the  $3\sigma$  detection threshold.

HCG 30 is one of the most H I deficient groups in our sample and previous observations failed to detect any H I emission in the galaxies making up its core. However, we detect two clump-like H I emission slightly offset from the optical centres of HCG30a and HCG30c as shown in Figure C.3. One clump is located at  $0.86'$  (15 kpc) from HCG30a, while the other one is at  $0.33'$  (6 kpc) from HCG30c. They could be the remains of stripped H I from HCG30a and HCG30c. The H I detection in HCG 30a remains spurious and unresolved despite being a large spiral galaxy. We show overview plots of HCG 30c in C.4. These plots were generated using the SoFiA Image Pipeline (SIP) by Hess K.M.<sup>1</sup> (Hess et al. 2024). As shown in the figure, the H I emission in HCG30c is faint and is barely resolved.

The H I emission corresponding to HCG 30b was split as three sources by SoFiA. We combined the three individual cubelettes from SoFiA using the MIRIAD task IMCOMB and re-derived the moment maps, which we show in Figure C.5. The moment one map presents apparent signs of rotation but the iso-velocity contours do not show the spider patterns expected from Sa galaxies. Instead, they show systematically convex curvatures. Note though that the emission along the minor axis is barely resolved. The global H I profile exhibits an enhanced intensity at either side of a more subdued central peak. However,

the overall S/N of the profile is low. The systemic velocity we got from SIP,  $4519 \text{ km s}^{-1}$ , corresponds well to the one quoted by Jones et al. (2023),  $4508 \text{ km s}^{-1}$ , from its optical redshift.

We show the 3D visualisation of HCG 30 in Figure C.6. The 3D plot does not show a hint of detection at the location of the core members. The tentative detection we observed in the moment maps needs to be confirmed by future more sensitive observations. In addition, the surrounding galaxies do not show any signs of morphological disturbance.

#### 4.6. HCG 90

##### 4.6.1. Data cube

The RA-velocity plot of HCG 90 is shown in the left panel of Figure D.1, indicating no obvious continuum residuals. The median noise values of the non-primary beam corrected cube as a function of velocity is presented in the middle panel of the figure. We compare the VLA and the MeerKAT global profile of HCG 90 in the right panel of Figure D.1. Since the VLA observations only detected H I emission in HCG 90a, the MeerKAT global profile appears much brighter than that of the VLA as MeerKAT detects emission both at the central part and in the vicinity of HCG 90.

We show example channel maps of the central part of HCG 90 in Figure D.2. More channel maps, covering a wider velocity range, can be downloaded here. The tail described previously appears as broken contours of low-column density H I, with the brightest contour found at  $2271$  to  $2293 \text{ km s}^{-1}$ , at the southern optical tail. No  $3\text{-}\sigma$  contour is found at the location of HCG 90b, HCG 90c, and HCG 90d.

The moment maps of HCG 90 are shown in Figure D.3. The maps indicate a previously undetected H I tail in the central region of HCG 90. When plotted against a deep DECaLS image, the H I tail seems to be aligned with the optical tail. It has a total mass of  $2.81 \times 10^8 M_{\odot}$ , and is about 128 kpc long. On projection, it is difficult to assess which members the tails are associated with. However, part of the tail coincides with the location of HCG90b and HCG90d. Previous H $\alpha$  kinematics by Plana et al. (1998) shows evidence of ongoing interaction between HCG 90b and HCG 90d, with HCG 90d acting as a gas provider. Spatially, the northern tail coincides more with the location of HCG 90d than that of HCG 90b. We also show in Figure D.3 a position-velocity map of the tail taken from a thick slice shown at the top right panel of the figure. A continuity in velocity is clearly visible, suggesting that this is not a projection of multiple features but rather a single, coherent structure. A more compact H I structure is found further north of HCG 90c, at the south western side of HCG 90a. We therefore hypothesise that the observed tail is part of a more extended structure connecting HCG 90c with the other members, which may have escaped our detection, or have already been dispersed by other processes such as ionisation or star formation. HCG 90a has been detected before by the VLA, and we also clearly detect it with MeerKAT.

Figure D.5 presents the 3D view of HCG 90. The tail we see in the moment map is also visible in the 3D plot and appears to be a tidal remnant of HCG 91c. This group might be a good candidate to look for diffuse H I components as the detection of this tidal fragment suggests that it is at a less advanced evolutionary stage than HCG 30 and HCG 97.

<sup>1</sup> <https://github.com/kmhess/SoFiA-image-pipeline>

#### 4.7. HCG 97

The RA-velocity plot of HCG 97 is shown in the left panel of Figure E.1, presenting some continuum residual emission that appears as positive and negative vertical stripes. These artefacts also manifest as increased noise levels starting around  $7500 \text{ km s}^{-1}$  and above as shown in the middle panel of the figure. The comparison between the VLA global profile and that of MeerKAT is presented in the right panel of Figure E.1. Another H I emission peak beyond the velocity covered by the VLA is detected by MeerKAT. The moment maps are shown in Figure E.2. Many galaxies are detected beyond the central part of HCG 97. However, no H I emission is detected in HCG 97a, HCG 97c, HCG 97d, and HCG 97e. Only HCG 97b is detected, whose approaching side was also detected by the VLA (Jones et al. 2023). Jones et al. (2023) suggested that HCG 97b might be disturbed since they only detected one side of the galaxy. However, we do not see any H I extension in our map despite the fact that MeerKAT detected the two sides of the galaxies. The receding part of this galaxy is indeed fainter as previously mentioned by Jones et al. (2023). HCG 97b is an edge-on spiral galaxy, but its velocity field is typical of a dwarf with solid body rotation curve. This is further corroborated by the position-velocity diagram shown in Figure E.2, which shows that HCG 97b has a very steep inner rotation curve, which most spirals with flat rotation curve also have (Bosma 1978). If this galaxy has a flat rotation curve, then we are only probing its inner disk, corresponding to the rising part of the rotation curve. Its outer disk might be too faint to be detected. Thus, we do not exclude the possibility that this galaxy is interacting.

Figure E.4 presents the 3D view of HCG 97. No signs of detection are observed at the location of the core members. Only HCG 97b is detected. The surrounding members are not morphologically disturbed. Our observations confirm that this group is at an advanced evolutionary stage.

## 5. Summary and conclusion

We have presented MeerKAT H I observations of six HCGs (3 phase 2 and 3 in phase 3), providing essential data to understand the transition between the two most evolved phases in the evolutionary sequence of these compact galaxy aggregations. We aimed to detect diffuse H I gas that was apparent in previous GBT observations but missed by the VLA telescope. Our observations have revealed significantly more extended tidal features in phase 2 groups compared to those detected by the VLA. In addition, we have detected new high surface brightness features in phase 3 groups. The presence of tidal features, such as H I tails, bridges, and clumps, suggests substantial gas loss into the IGrM due to gravitational interactions. When derived within the field of view of GBT, our measured H I flux is similar to that of the GBT. However, we have not detected the diffuse H I component apparent in previous GBT spectra for phase 3 groups despite MeerKAT's superb sensitivity. This indicates that part of the missing H I could be too diffuse to be detected by MeerKAT and the rest might be ionised. Numerous surrounding galaxies have been detected for both phase 2 and phase 3 groups, most of which are normal disk galaxies. This suggests that these groups might be embedded in larger structures. MeerKAT detected significantly more extended H I gas in Phase 2 groups than the VLA, thanks to its superior short baseline coverage. Thus, a single-dish telescope such as FAST is expected to detect H I at even larger angular scales beyond MeerKAT's coverage. Apart from data cubes, source catalogues, and moment maps, we have released 3D visualisation

of our data. This offers a more advanced approach to visually inspect different H I features, which can help in separating the complex substructures present in phase 2 groups.

## 6. Data availability

All the necessary scripts and data inputs are released along with this paper and can be found at <https://github.com/ianjarog/hcg-data-paper>; the instructions to download and process the data are also given there.

*Acknowledgements.* Authors RI, LVM, AS, IL, CC, TW, BN, JM, SSE, JG acknowledge financial support from the grant PID2021-123930OB-C21 funded by MICIU/AEI/ 10.13039/501100011033 and by ERDF/EU, and the grant CEX2021-001131-S funded by MICIU/AEI/ 10.13039/501100011033, and the grant TED2021-130231B-I00 funded by MICIU/AEI/ 10.13039/501100011033 and by the European Union NextGenerationEU/PRTR, and acknowledge the Spanish Prototype of an SRC (espSRC) service and support funded by the Ministerio de Ciencia, Innovación y Universidades (MICIU), by the Junta de Andalucía, by the European Regional Development Funds (ERDF) and by the European Union NextGenerationEU/PRTR. The espSRC acknowledges financial support from the Agencia Estatal de Investigación (AEI) through the "Center of Excellence Severo Ochoa" award to the Instituto de Astrofísica de Andalucía (IAA-CSIC) (SEV-2017-0709) and from the grant CEX2021-001131-S funded by MICIU/AEI/ 10.13039/501100011033. Part of BN's work was supported by the grant PTA2023-023268-I funded by MICIU/AEI/ 10.13039/501100011033 and by ESF+. IL also acknowledges financial support from PRE2021-100660 funded by MICIU/AEI/ 10.13039/501100011033 and by ESF+. JMS acknowledge financial support from the Spanish state agency MCIN/AEI/10.13039/501100011033 and by 'ERDF A way of making Europe' funds through research grant PID2022-140871NB-C22. MCIN/AEI/10.13039/501100011033 has also provided additional support through the Centre of Excellence María de Maeztu's award for the Institut de Ciències del Cosmos at the Universitat de Barcelona under contract CEX2019-000918-M. JR acknowledges financial support from the Spanish Ministry of Science and Innovation through the project PID2022-138896NB-C55. MEC acknowledges the support of an Australian Research Council Future Fellowship (Project No. FT170100273) funded by the Australian Government. TW acknowledges financial support from the grant CEX2021-001131-S funded by MICIU/AEI/ 10.13039/501100011033, from the coordination of the participation in SKA-SPAIN, funded by the Ministry of Science, Innovation and Universities (MICIU). A. del Olmo and J. Perea acknowledge financial support from the Spanish MCIU through project PID2022-140871NB-C21 by 'ERDF A way of making Europe', and the Severo Ochoa grant CEX2021- 515001131-S funded by MCIN/AEI/10.13039/501100011033. JMS acknowledge financial support from the Spanish state agency MCIN/AEI/10.13039/501100011033 and by 'ERDF A way of making Europe' funds through research grant PID2022-140871NB-C22. MCIN/AEI/10.13039/501100011033 has also provided additional support through the Centre of Excellence María de Maeztu's award for the Institut de Ciències del Cosmos at the Universitat de Barcelona under contract CEX2019-000918-M. EA and AB gratefully acknowledge support from the Centre National d'Études Spatiales (CNES), France. RGB acknowledges financial support from the Severo Ochoa grant CEX2021-001131-S funded by MCIN/AEI/ 10.13039/501100011033 and PID2022-141755NB-I00. JM acknowledges financial support from grant PID2023-147883NB-C21, funded by MCIU/AEI/ 10.13039/501100011033 OMS's research is supported by the South African Research Chairs Initiative of the Department of Science and Technology and National Research Foundation (grant No. 81737). The MeerKAT telescope is operated by the South African Radio Astronomy Observatory, which is a facility of the National Research Foundation, an agency of the Department of Science and Innovation.

## References

- Alatalo, K., Appleton, P. N., Lisenfeld, U., et al. 2015, *ApJ*, 812, 117. doi:10.1088/0004-637X/812/2/117
- Amram, P., Plana, H., Mendes de Oliveira, C., et al. 2003, *A&A*, 402, 865. doi:10.1051/0004-6361:20030034
- Amram, P., Mendes de Oliveira, C., Plana, H., et al. 2004, *ApJ*, 612, L5. doi:10.1086/424482
- Amram, P., Mendes de Oliveira, C., Plana, H., et al. 2007, *A&A*, 471, 753. doi:10.1051/0004-6361:20054069
- Barnes, D. G. & Webster, R. L. 2001, *MNRAS*, 324, 859. doi:10.1046/j.1365-8711.2001.04273.x



- Bitsakis, T., Charmandaris, V., Appleton, P. N., et al. 2014, *A&A*, 565, A25. doi:10.1051/0004-6361/201323349
- Borthakur, S., Yun, M. S., & Verdes-Montenegro, L. 2010, *ApJ*, 710, 385. doi:10.1088/0004-637X/710/1/385
- Bosma, A. 1978, Ph.D. Thesis
- Cluver, M. E., Appleton, P. N., Ogle, P., et al. 2013, *ApJ*, 765, 93. doi:10.1088/0004-637X/765/2/93
- Da Rocha, C., Mieske, S., Georgiev, I. Y., et al. 2011, *A&A*, 525, A86. doi:10.1051/0004-6361/201015353
- Desjardins, T. D., Gallagher, S. C., Tzanavaris, P., et al. 2013, *ApJ*, 763, 121. doi:10.1088/0004-637X/763/2/121
- Dey, A., Schlegel, D. J., Lang, D., et al. 2019, *AJ*, 157, 168. doi:10.3847/1538-3881/ab089d
- Egenthaler, P., Ploechinger, S., Verdugo, M., et al. 2015, *MNRAS*, 451, 2793. doi:10.1093/mnras/stv1037
- Garrido, J., Darriba, L., Sánchez-Expósito, S., et al. 2022, *Journal of Astronomical Telescopes, Instruments, and Systems*, 8, 011004. doi:10.1117/1.JATIS.8.1.011004
- Gómez-Espinoza, D. A., Torres-Flores, S., Firpo, V., et al. 2023, *MNRAS*, 522, 2655. doi:10.1093/mnras/stad1084
- Heckman, T. M., Blitz, L., Wilson, A. S., et al. 1989, *ApJ*, 342, 735. doi:10.1086/167633
- Hess, K. M., Cluver, M. E., Yahya, S., et al. 2017, *MNRAS*, 464, 957. doi:10.1093/mnras/stw2338
- Kelley M. Hess, paoloserra, Leon Boschman, Austin Shen, & Julia H. (2024). kmhess/SoFiA-image-pipeline: v1.3.5 (v1.3.5). Zenodo. <https://doi.org/10.5281/zenodo.14016958>
- Hickson, P. 1982, *ApJ*, 255, 382. doi:10.1086/159838
- Hickson, P., Kindl, E., & Auman, J. R. 1989, *ApJS*, 70, 687. doi:10.1086/191354
- Hickson, P., Mendes de Oliveira, C., Huchra, J. P., et al. 1992, *ApJ*, 399, 353. doi:10.1086/171932
- Hu, D., Zajaček, M., Werner, N., et al. 2023, *MNRAS*. doi:10.1093/mnras/stad3219
- Huchtmeier, W. K. 1997, *A&A*, 325, 473
- Huchtmeier, W. K. & Tammann, G. A. 1992, *A&A*, 257, 455
- Iglesias-Paramo, J. & Vilchez, J. M. 1997, *ApJ*, 479, 190. doi:10.1086/512789
- Iglesias-Paramo, J. & Vilchez, J. M. 2001, *ApJ*, 550, 204. doi:10.1086/319710
- Jones, M. G., Verdes-Montenegro, L., Damas-Segovia, A., et al. 2019, *A&A*, 632, A78. doi:10.1051/0004-6361/201936349
- Johnson, K. E., Vacca, W. D., Leitherer, C., et al. 1999, *AJ*, 117, 1708. doi:10.1086/300800
- Jones, M. G., Verdes-Montenegro, L., Moldon, J., et al. 2023, *A&A*, 670, A21. doi:10.1051/0004-6361/202244622
- Józsa, G. I. G., White, S. V., Thorat, K., et al. 2020, *Astronomical Data Analysis Software and Systems XXIX*, 527, 635. doi:10.48550/arXiv.2006.02955
- Kenyon, J. S., Smirnov, O. M., Grobler, T. L., et al. 2018, *MNRAS*, 478, 2399. doi:10.1093/mnras/sty1221
- Labadie-García, I., Garrido, J., Verdes-Montenegro, L. 2024, Zenodo, v0.2. doi:10.5281/zenodo.13254756
- Lisenfeld, U., Appleton, P. N., Cluver, M. E., et al. 2014, *A&A*, 570, A24. doi:10.1051/0004-6361/201423632
- López-Sánchez, Á. R., Esteban, C., & Rodríguez, M. 2004, *ApJS*, 153, 243. doi:10.1086/420897
- Makhathini, S. 2018, Ph.D. Thesis
- Mauch, T., Cotton, W. D., Condon, J. J., et al. 2020, *ApJ*, 888, 61. doi:10.3847/1538-4357/ab5d2d
- Mazzarella, J. M. & Boroson, T. A. 1993, *ApJS*, 85, 27. doi:10.1086/191754
- Mendes de Oliveira, C., Amram, P., Plana, H., et al. 2003, *AJ*, 126, 2635. doi:10.1086/379295
- Mendes de Oliveira, C. L., Temporin, S., Cypriano, E. S., et al. 2006, *AJ*, 132, 570. doi:10.1086/504595
- Meurer, G. R., Hanish, D. J., Ferguson, H. C., et al. 2006, *ApJS*, 165, 307. doi:10.1086/504685
- Miah, J. A., Sharples, R. M., & Cho, J. 2015, *MNRAS*, 447, 3639. doi:10.1093/mnras/stu2735
- Mölder, F., Jablonski, K.P., Letcher, B., Hall, M.B., Tomkins-Tinch, C.H., Sochat, V., Forster, J., Lee, S., Twardziok, S.O., Kanitz, A., Wilm, A., Holtgrewe, M., Rahmann, S., Nahnsen, S., Köster, J., 2021. Sustainable data analysis with Snakemake. *F1000Res* 10, 33.
- Ordenes-Briceño, Y., Taylor, M. A., Puzia, T. H., et al. 2016, *MNRAS*, 463, 1284. doi:10.1093/mnras/stw2066
- Offringa, A. R., van de Gronde, J. J., & Roerdink, J. B. T. M. 2012, *A&A*, 539, A95. doi:10.1051/0004-6361/201118497
- Offringa, A. R., McKinley, B., Hurley-Walker, N., et al. 2014, *MNRAS*, 444, 606. doi:10.1093/mnras/stu1368
- Oosterloo, T. & Iovino, A. 1997, *The Nature of Elliptical Galaxies; 2nd Stromlo Symposium*, 116, 358
- O'Sullivan, E., Zezas, A., Vrtilik, J. M., et al. 2014, *ApJ*, 793, 73. doi:10.1088/0004-637X/793/2/73
- Pildis, R. A., Bregman, J. N., & Schombert, J. M. 1995, *AJ*, 110, 1498. doi:10.1086/117623
- Palumbo, G. G. C., Saracco, P., Hickson, P., et al. 1995, *AJ*, 109, 1476. doi:10.1086/117377
- Plana, H., Mendes de Oliveira, C., Amram, P., et al. 1998, *AJ*, 116, 2123. doi:10.1086/300621
- Rasmussen, J., Ponman, T. J., Verdes-Montenegro, L., et al. 2008, *MNRAS*, 388, 1245. doi:10.1111/j.1365-2966.2008.13451.x
- Richer, M. G., Georgiev, L., Rosado, M., et al. 2003, *A&A*, 397, 99. doi:10.1051/0004-6361:20021394
- Román, J., Jones, M. G., Montes, M., et al. 2021, *A&A*, 649, L14. doi:10.1051/0004-6361/202141001
- Rubin, V. C., Hunter, D. A., & Ford, W. K. 1990, *ApJ*, 365, 86. doi:10.1086/169459
- Serra, P., Westmeier, T., Giese, N., et al. 2015, *MNRAS*, 448, 1922. doi:10.1093/mnras/stv079
- Serra, P., Maccagni, F. M., Kleiner, D., et al. 2023, *A&A*, 673, A146. doi:10.1051/0004-6361/202346071
- Torres-Flores, S., Mendes de Oliveira, C., Amram, P., et al. 2015, *ApJ*, 798, L24. doi:10.1088/2041-8205/798/1/L24
- Verdes-Montenegro, L., Yun, M., Perea, J., et al. 1997, *Dark and Visible Matter in Galaxies and Cosmological Implications*, 117, 530
- Verdes-Montenegro, L., Yun, M. S., Perea, J., et al. 1998, *ApJ*, 497, 89. doi:10.1086/305454
- Verdes-Montenegro, L., Yun, M. S., Williams, B. A., et al. 2001, *A&A*, 377, 812. doi:10.1051/0004-6361:20011127
- Verdes-Montenegro, L., Del Olmo, A., Yun, M. S., et al. 2005, *A&A*, 430, 443. doi:10.1051/0004-6361:20047084
- Verdes-Montenegro, L., Yun, M. S., Borthakur, S., et al. 2007, *New A Rev.*, 51, 87. doi:10.1016/j.newar.2006.10.008
- Verdes-Montenegro, L., Vogt, F., Aubery, C., et al. 2017, *Formation and Evolution of Galaxy Outskirts*, 321, 241. doi:10.1017/S1743921316011637
- Véron-Cetty, M.-P. & Véron, P. 2010, *A&A*, 518, A10. doi:10.1051/0004-6361/201014188
- Vílchez, J. M. & Iglesias-Paramo, J. 1998, *ApJS*, 117, 1. doi:10.1086/313115
- Vogt, F. P. A., Dopita, M. A., Borthakur, S., et al. 2015, *MNRAS*, 450, 2593. doi:10.1093/mnras/stv749
- Vogt, F. P. A., Owen, C. I., Verdes-Montenegro, L., et al. 2016, *ApJ*, 818, 115. doi:10.3847/0004-637X/818/2/115
- Wang, J., Yang, D., Oh, S.-H., et al. 2023, *ApJ*, 944, 102. doi:10.3847/1538-4357/acafe8
- Westmeier, T., Kitaef, S., Pallot, D., et al. 2021, *MNRAS*, 506, 3962. doi:10.1093/mnras/stab1881
- Williams, B. A. & Rood, H. J. 1987, *ApJS*, 63, 265. doi:10.1086/191165
- White, P. M., Bothun, G., Guerrero, M. A., et al. 2003, *ApJ*, 585, 739. doi:10.1086/346075
- Yun, M. S., Verdes-Montenegro, L., del Olmo, A., et al. 1997, *ApJ*, 475, L21. doi:10.1086/310458

## Appendix A: Additional figures of HCG 31

### Appendix A.1: Channel maps

Figure A.1 shows example channel maps from the primary beam corrected data cube of HCG 31, overlaid on DECaLS DR10 R-band optical images.

### Appendix A.2: Moment maps

Figure A.2 shows the column density maps and moment one (velocity field) of HCG 31. The left panel highlights the large-scale structure of the group, whereas the right panel shows its central part. To better illustrate the previously identified tidal dwarf galaxies within HCG 31 (see section 4.3), we present in Figure A.3 a higher-resolution view of the group's central region, derived from a data cube at  $15.47'' \times 11.86''$ .

### Appendix A.3: 3D visualisation

We present in Figure A.4 a three-dimensional visualisation of HCG 31. The left panel displays iso-surfaces corresponding to high-column-density gas, emphasising the group's densest structures, while the right panel highlights the diffuse low-column-density H I gas. Blue circles mark the positions of the member galaxies. The 2D grayscale background is a DeCaLS R-band optical image of the group. An interactive version of these 3D cubes is publicly accessible at <https://amiga.iaa.csic.es/x3d-menu/>.

## Appendix B: Additional figures of HCG 91

### Appendix B.1: Noise properties and global profiles

The RA-velocity plot of HCG 91 is shown in the first panel of Figure B.1. The middle panel shows the median noise levels in each RA-DEC slice of the non primary beam corrected data cube as a function of velocity. The horizontal dashed line indicates the global median noise. The right panel compares the MeerKAT H I integrated spectra with archival VLA measurements from (Jones et al. 2023), where the vertical dotted lines denote the systemic velocities of the galaxies in the group's core. All spectra were extracted from regions containing only genuine H I emission.

### Appendix B.2: Channel maps

Figure B.2 presents the channel maps of HCG 91 overlaid on DECaLS DR10 I-band optical image. More channel maps, covering a larger velocity range, can be found [here](#).

### Appendix B.3: Moment maps

The column density maps of HCG 91 is shown in Figure B.3. The left panels show all detected sources within the field of view of MeerKAT. The right panels present the central part of the group. The H I maps are overlaid on DECaLS DR10 I-band optical images.

### Appendix B.4: Velocity fields of the core members of HCG 91

The velocity fields of the galaxies in the core of HCG 91 are shown in Figure B.4. The grayscale images show optical I-band DeCaLS DR10 data.

### Appendix B.5: 3D visualisation

The 3D visualisation of HCG 91 is presented in Figure B.5. The left panel displays iso-surfaces that highlight regions of high H I column density, while the right panel overlays areas of low and high column density. The blue circles mark the positions of the group's member galaxies, and the 2D grayscale background is a DECaLS R-band image. An interactive version of these cubes can be found at <https://amiga.iaa.csic.es/x3d-menu/>.

## Appendix C: Extra figures of HCG 30

### Appendix C.1: Noise properties and global profiles

Figure C.1 illustrates the noise properties in HCG 30 and compares the MeerKAT and VLA integrated spectra of the group. The left panel displays the RA-velocity plot. The middle panel shows the median noise levels across individual RA-DEC slices of the non primary beam corrected data cube, with a horizontal dashed line indicating the global median noise. The right panel compares the H I integrated spectrum derived from the MeerKAT data (blue solid line) with the VLA measurement from Jones et al. (2023) (red solid line). The vertical dotted lines mark the systemic velocities of the core galaxies. The spectra were extracted from regions containing only genuine H I emission.

### Appendix C.2: Channel maps

Figure C.2 shows example channel maps from the primary beam corrected data cube of HCG 30. Additional channel maps can be retrieved from <https://zenodo.org/records/14856489>.

### Appendix C.3: Moment maps

Figure C.3 presents the H I moment maps of HCG 30. The left panels show all H I sources detected by SoFiA within the MeerKA field of view, while the right panels display zoomed-in views of the group's core. The top panels show column density maps overlaid on DECaLS DR10 R-band optical images. The bottom panels display the moment-one (velocity field) map for each detected source, highlighting the rotational signatures of the surrounding galaxies.

### Appendix C.4: The core members of HCG 30

Our tentative detection of H I in the core members of HCG 30 is illustrated in Figure C.4 and Figure C.5. These plots were generated by the SoFiA Image Pipeline<sup>2</sup>(Hess et al. 2024), an automated tool that takes as an input a SoFiA-generated source catalogue and produces overview plots of the H I properties of the sources. Figure C.4 and Figure C.5 show H I contours overlaid on DeCaLS false-colour images, H I moment maps, pixel-by-pixel signal-to-noise ratio maps, position-velocity diagrams, and global H I spectra.

### Appendix C.5: 3D visualisation

Figure C.6 presents a 3D visualisation of HCG 30. The member galaxies are indicated by the blue circles, and the grayscale background is a DECaLS R-band optical image. An interactive 3D version of these cubes can be found at <https://amiga.iaa.csic.es/x3d-menu/>.

<sup>2</sup> <https://github.com/kmhess/SoFiA-image-pipeline>

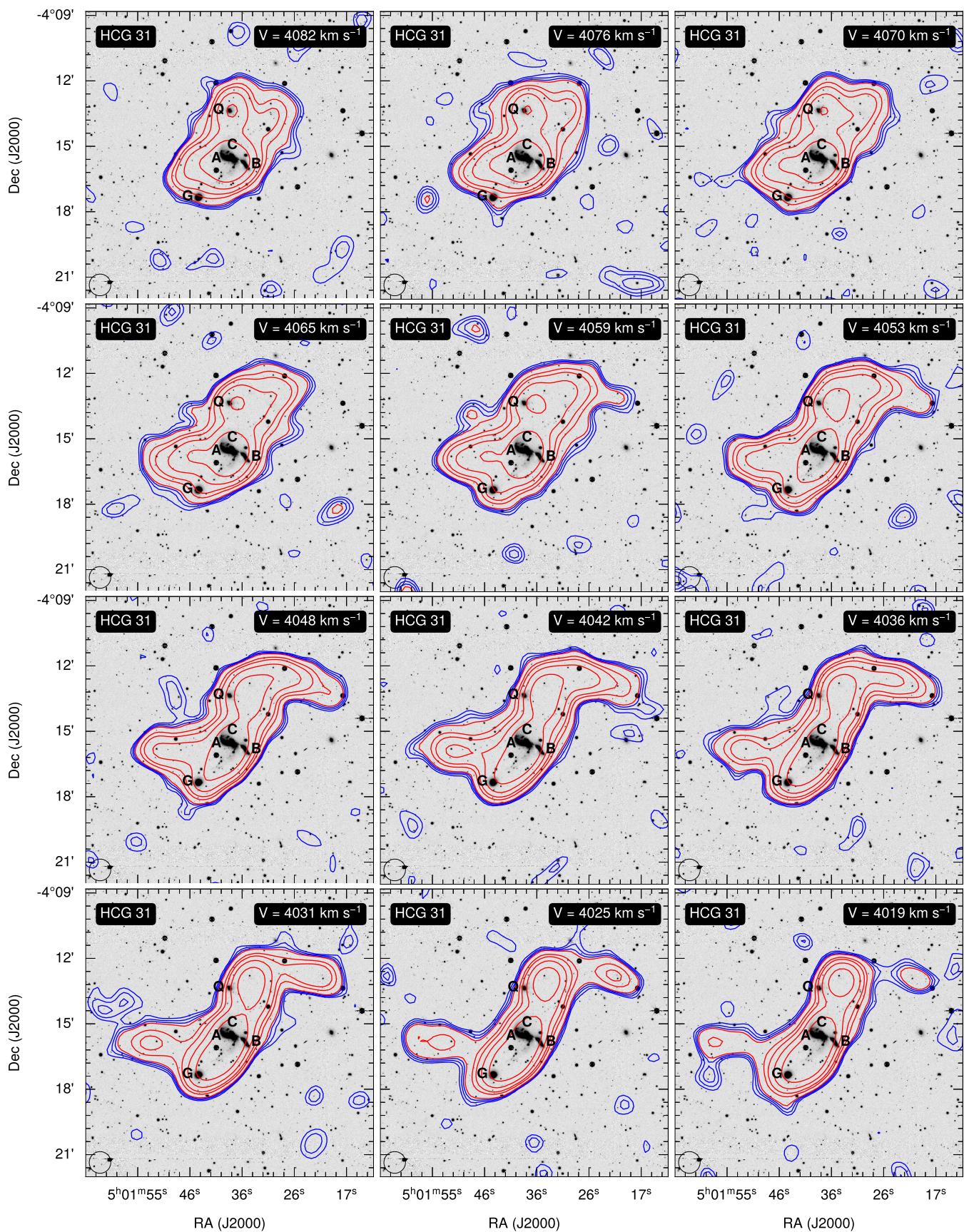


Fig. A.1: Example channel maps of the primary beam corrected cube of HCG 31 overlaid on DECaLS DR10 R-band optical images. Contour levels are (1.5, 2, 2.5, 3, 6, 9, 16, 32) times the median noise level in the cube (0.71 mJy beam<sup>-1</sup>). The blue colours show contour levels below  $3\sigma$ ; the red colours represent contour levels at  $3\sigma$ , or higher. More channel maps are available [online](#).

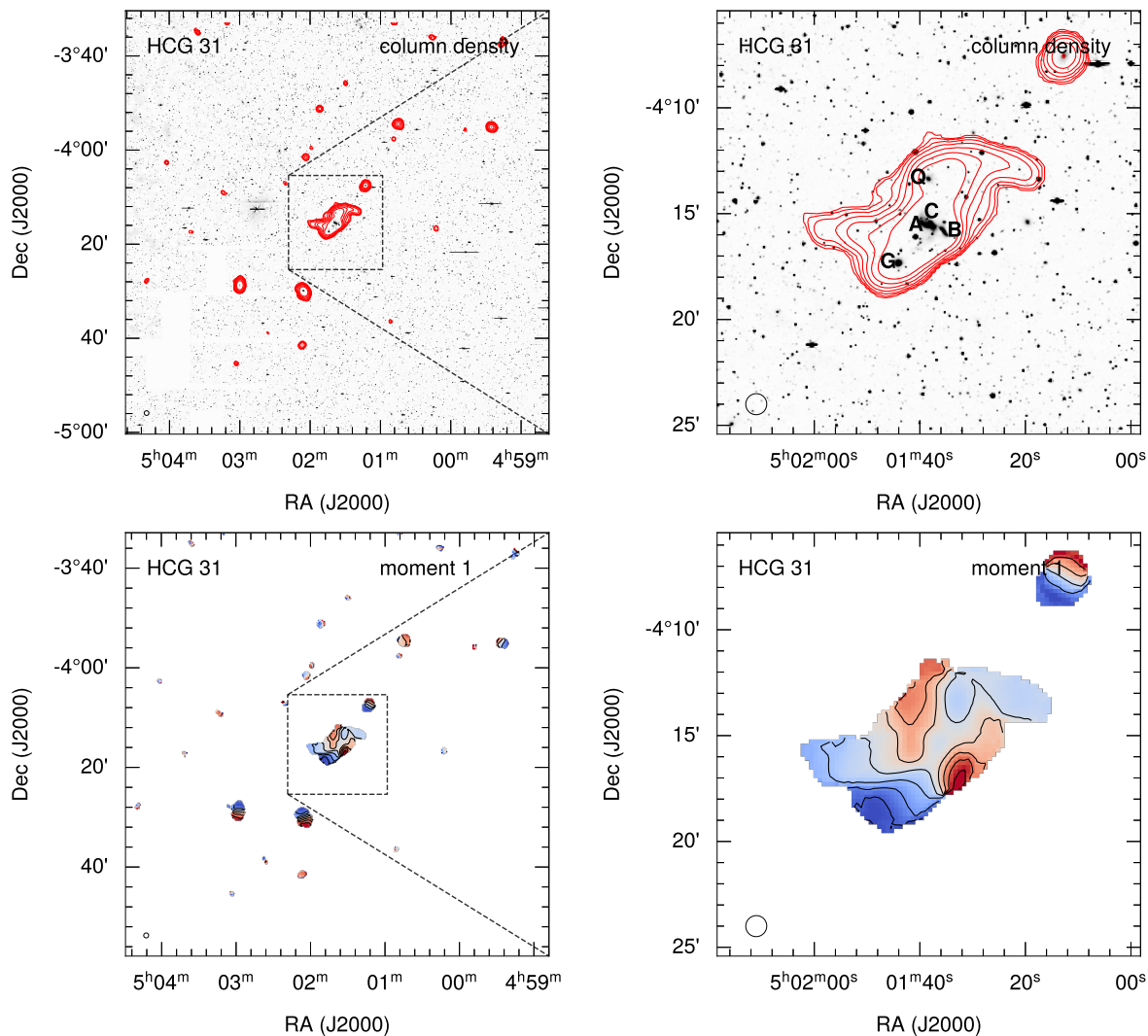


Fig. A.2: H I Moment maps of HCG 31. Left panels show all sources detected by SoFiA. The right panels show sources within the rectangular box shown on the left to better show the central part of the group. The top panels show the column density maps with contour levels of  $(4.0 \times 10^{18}, 8.0 \times 10^{18}, 1.6 \times 10^{19}, 3.2 \times 10^{19}, 6.4 \times 10^{19}, 1.3 \times 10^{20}, 2.6 \times 10^{20}) \text{ cm}^{-2}$ . The contours are overlaid on DECaLS DR10 R-band optical images. The bottom panels show the moment one map. Each individual source has its own colour scaling and contour levels to highlight any rotational component.

## Appendix D: Supplementary figures of HCG 90

### Appendix D.1: Noise properties and global profiles

Figure D.1 shows the noise variations and global profiles of HCG 90. The left panel shows a RA-velocity slice. The middle panel plots the median noise levels per RA-DEC slice. The horizontal dashed line marks the overall median noise level. The right panel presents the MeerKAT integrated spectrum (blue solid line) compared with the VLA data (red solid line) originally presented by Jones et al. (2023). The vertical dotted lines indicate the systemic velocities of the galaxies in the core of the group.

### Appendix D.2: Channel maps

Figure D.2 displays representative channel maps from the primary beam corrected data cube of HCG 90, superimposed on enhanced DECaLS optical images. To enhance faint optical fea-

tures, G- and R-band images were combined, and pixel scaling was adjusted. The rest of the channel maps can be found [here](#).

### Appendix D.3: Moment maps

Figure D.3 shows the column density and moment one (velocity field) maps of HCG 90. The left panels present all sources detected by SoFiA, whereas the right panels focus on the central region. The top panels overlay H I column density contours on DECaLS optical images. The bottom panels display the velocity field with individual colour scalings for each source to highlight the rotational patterns of the surrounding galaxies.

### Appendix D.4: H I tails in HCG 90

Figure D.4 presents an overview plots of the H I tails in HCG 90. The top-left panel displays the H I column density map, with the blue region marking the slice used to derive the position-velocity diagram in the bottom-left panel of the figure. The top-centre

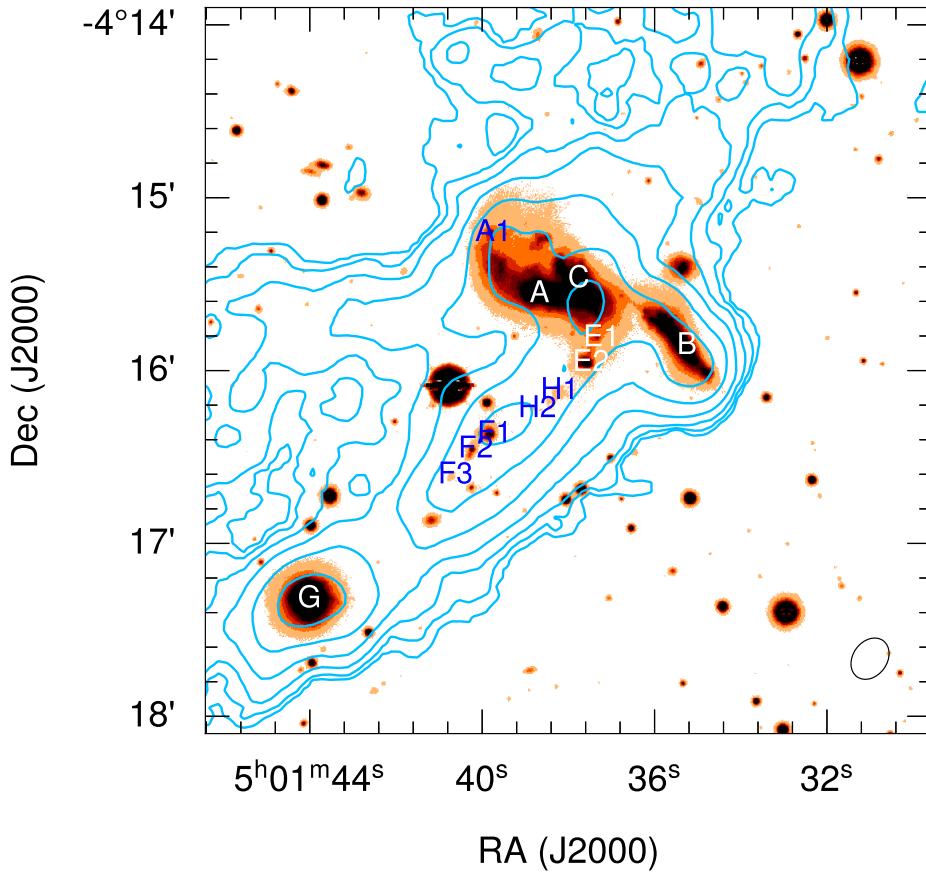


Fig. A.3: Column density map of the central part of HCG 31 from a  $15.47'' \times 11.86''$  datacube, overlaid on DECaLS filter optical images to highlight the core members. The contour levels are  $(5.96 \times 10^{19}, 1.19 \times 10^{20}, 2.38 \times 10^{20}, 4.77 \times 10^{20}, 9.53 \times 10^{20}, 1.91 \times 10^{21}, 3.20 \times 10^{21}) \text{ cm}^{-2}$ .

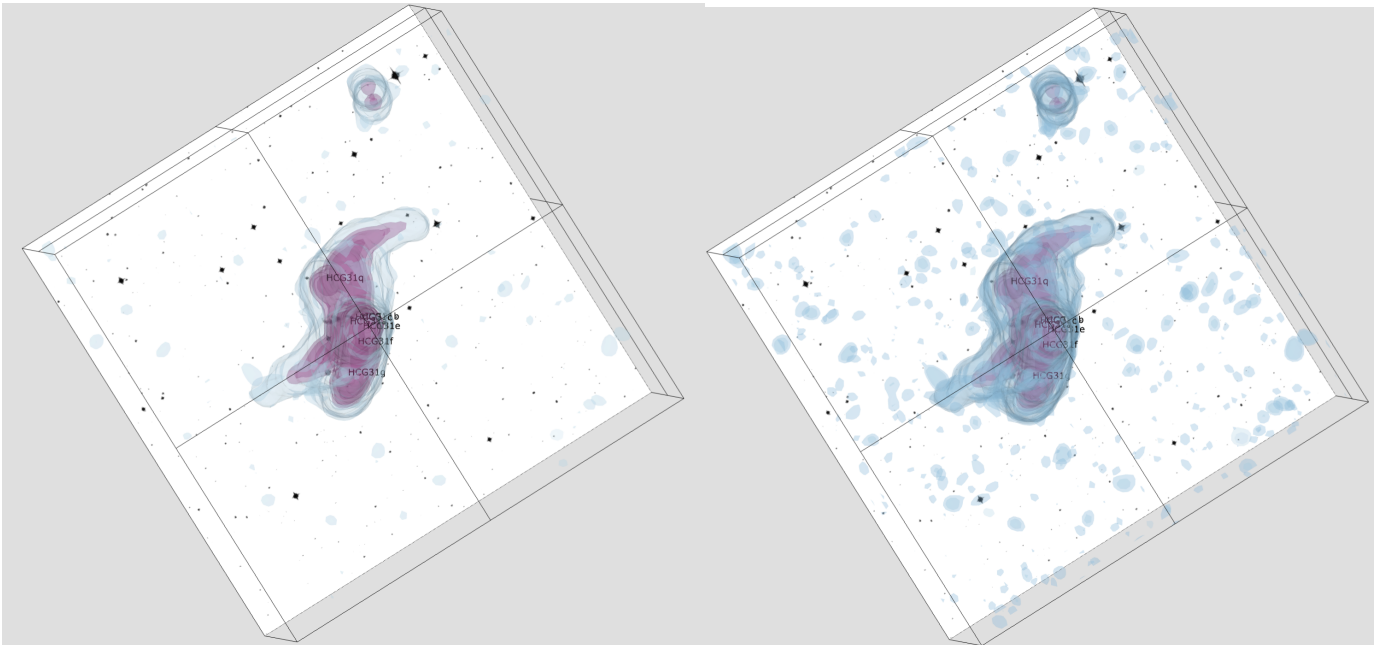


Fig. A.4: 3D visualisation of HCG 31. The left panel shows iso-surface level highlighting the high-column density gas. The right panel showcases the low-column density H I gas. The blue circles indicate the position of the member galaxies. The 2D grayscale image is a DeCaLS R-band optical image of the group. The online version of the cubes are available at <https://amiga.iaa.csic.es/x3d-menu/>.

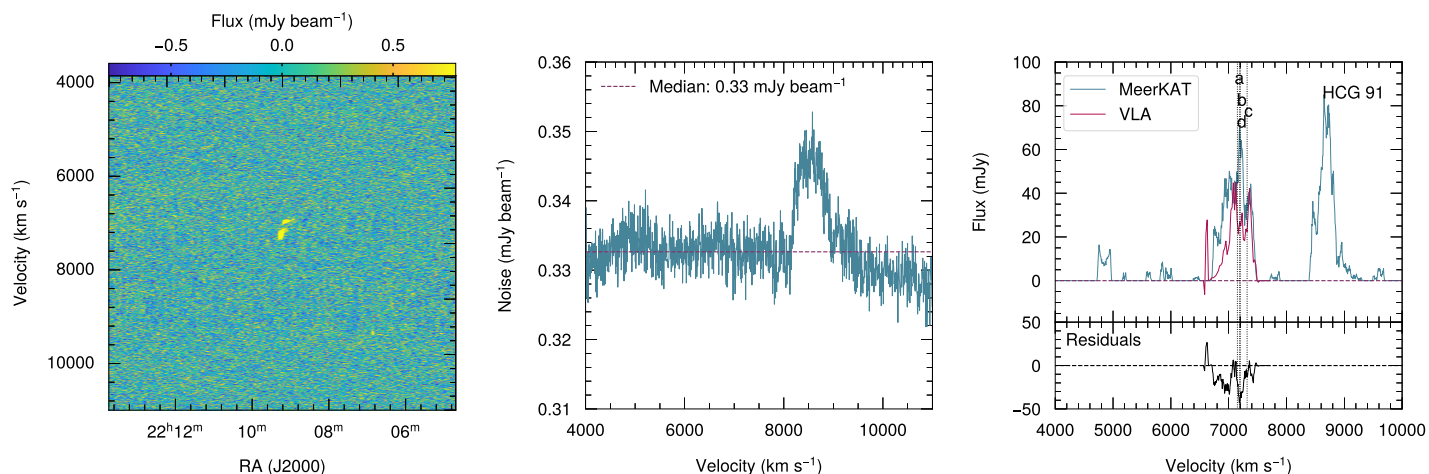


Fig. B.1: Left panel: velocity vs right ascension of HCG 91. Middle panel: median noise values of each RA-DEC slice of the non-primary beam corrected 60'' data cube of HCG 91 as a function of velocity. The horizontal dashed line indicates the median of all the noise values from each slice. Right panel: the blue solid lines indicates the MeerKAT integrated spectrum of HCG 91; the red solid line indicates VLA integrated spectrum of the group derived by (Jones et al. 2023). The vertical dotted lines indicate the velocities of the galaxies in the core of the group. The spectra have been extracted from areas containing only genuine H I emission.

panel shows the velocity field (moment-1 map), and the top-right panel presents the signal-to-noise ratio map. The bottom panels show a position-velocity diagram and a (smoothed) global profile of the tails.

#### Appendix D.5: 3D visualisation

Figure D.5 presents a 3D visualisation of HCG 90, where the blue circles mark the positions of the member galaxies. The background image is a DeCaLS R-band optical image of the group. An interactive version of these 3D cubes is available online at <https://amiga.iaa.csic.es/x3d-menu/>.

#### Appendix E.4: 3D visualisation

Figure E.4 shows a 3D visualisation of HCG 97. The blue circles mark the member galaxies and the 2D grayscale background image is a DeCaLS R-band optical data. An interactive version of the data cubes is also accessible at <https://amiga.iaa.csic.es/x3d-menu/>.

## Appendix E: Additional figures of HCG 97

### Appendix E.1: Noise properties and global profiles

Figure E.1 shows the RA-velocity plot of HCG 97 (left), the median noise level across the velocity channels (middle), and the MeerKAT and VLA integrated spectra (right).

### Appendix E.2: Moment maps

Figure E.2 presents the column density maps (top panels) and moment one (bottom panels) maps of HCG 97. The left panels show all sources detected by SoFiA within the MeerKAT field of view, whereas the right panels present zoomed-in views of the group's centre. The grayscale images are DeCaLS R-band optical data.

### Appendix E.3: H I in HCG 97b

Overview plots of the H I in HCG 97b are shown in Figure E.3. These images were generated by SIP, showing moment maps, signal-to-noise ratio, position-velocity diagrams and an integrated spectrum.

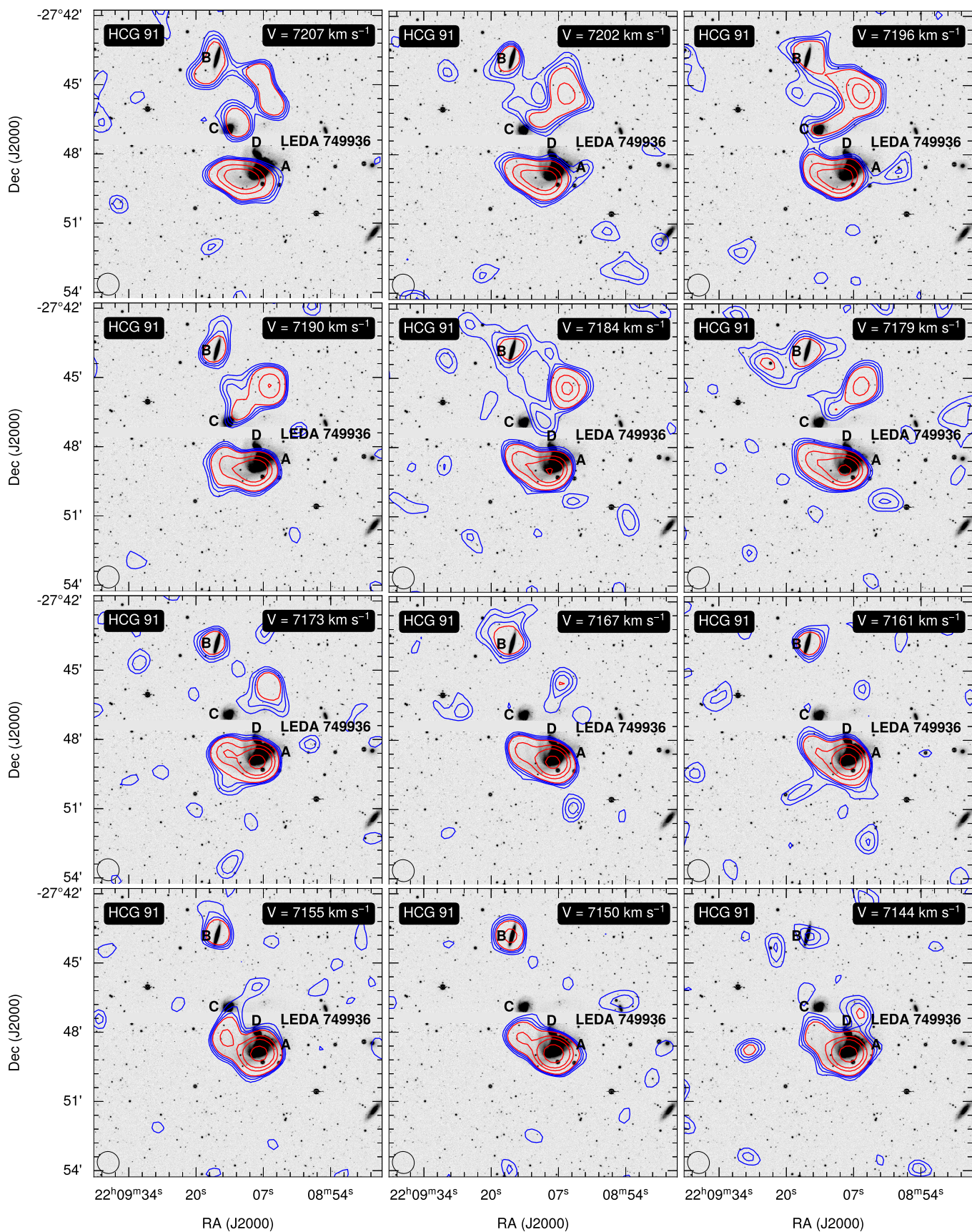


Fig. B.2: Example channel maps of the primary beam corrected cube of HCG 91 overlaid on DECaLS DR10 I-band optical image. Contour levels are (1.5, 2, 2.5, 3, 6, 9, 16, 32) times the median noise level in the cube (0.69 mJy beam<sup>-1</sup>). The blue colours show contour levels below  $3\sigma$ ; the red colours represent contour levels at  $3\sigma$ , or higher. Additional channel maps can be downloaded [here](#).

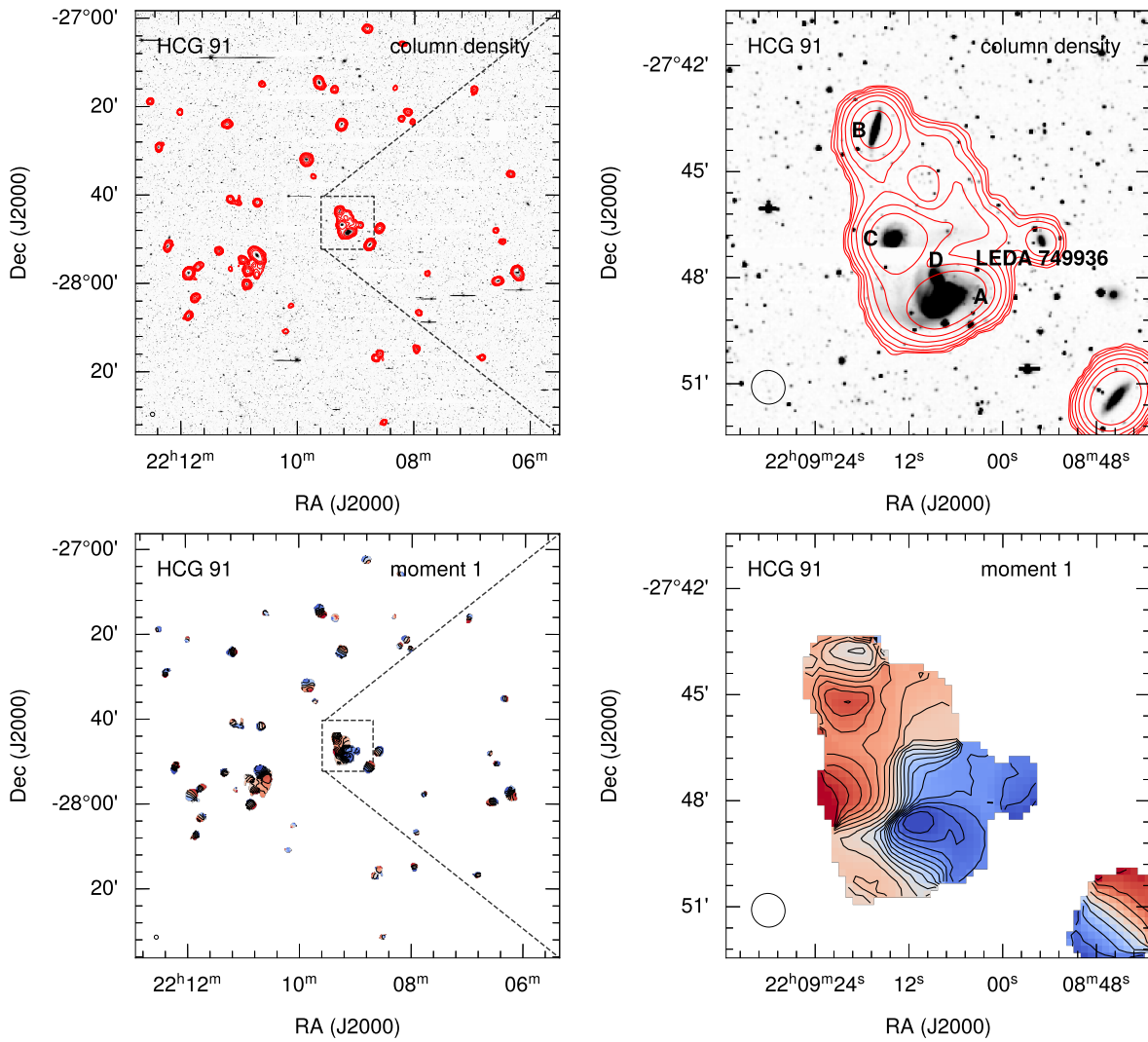


Fig. B.3: H I Moment maps of HCG 91. Left panels show all sources detected by SoFiA. The right panels show sources within the rectangular box shown on the left to better show the central part of the group. The top panels show the column density maps with contour levels of ( $4.6 \times 10^{18}$ ,  $9.2 \times 10^{18}$ ,  $1.8 \times 10^{19}$ ,  $3.7 \times 10^{19}$ ,  $7.4 \times 10^{19}$ ,  $1.5 \times 10^{20}$ ,  $3.0 \times 10^{20}$ )  $\text{cm}^{-2}$ . The contours are overlaid on DECaLS DR10 I-band optical images. The bottom panels show the moment one map. Each individual source has its own colour scaling and contour levels to highlight any rotational component.



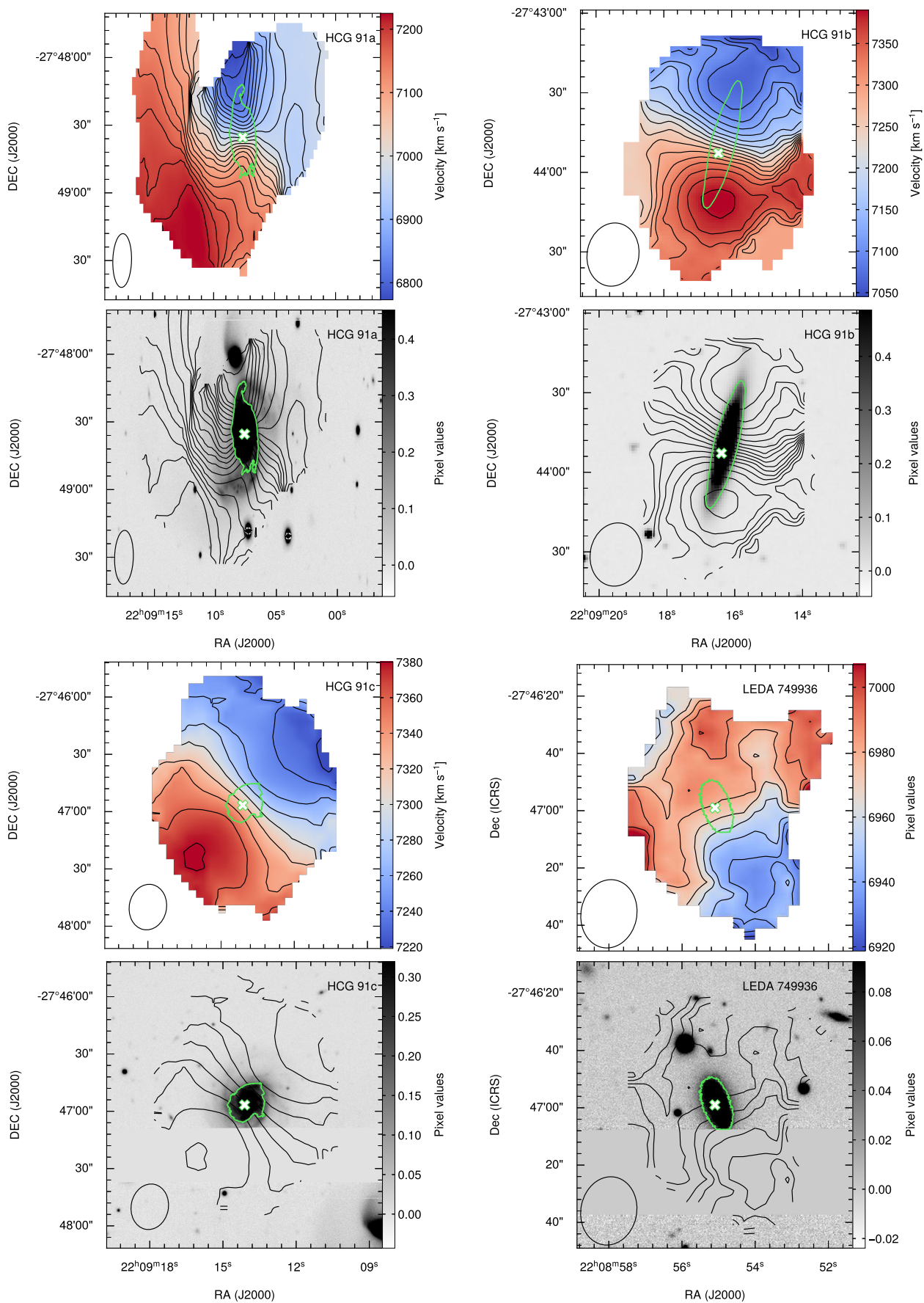


Fig. B.4: H I Velocity fields of the galaxies in the core of HCG 91. The grayscale images show DeCaLS DR10 I-band optical data. The crosses indicate the optical centre, whereas the green contours highlight the optical disk.

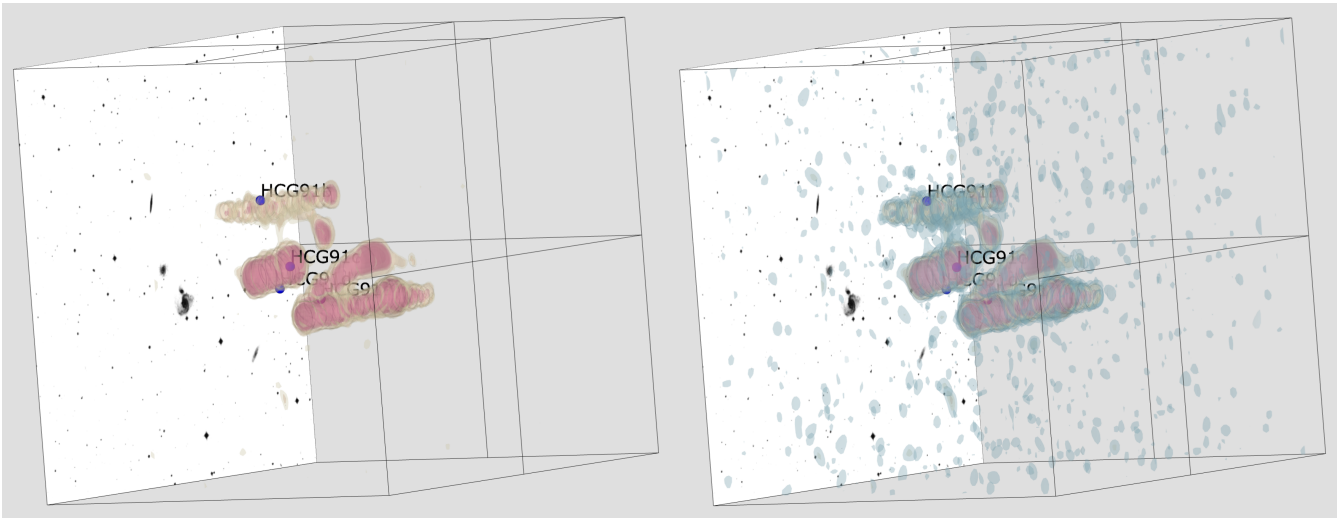


Fig. B.5: 3D visualisation of HCG 91. The left panel shows iso-surface level highlighting the high-column density gas. The right panel showcases the low-column density H I gas. The blue circles indicate the position of the member galaxies. The 2D grayscale image is a DeCaLS R-band optical image of the group. The online version of the cubes are available at <https://amiga.iaa.csic.es/x3d-menu/>.

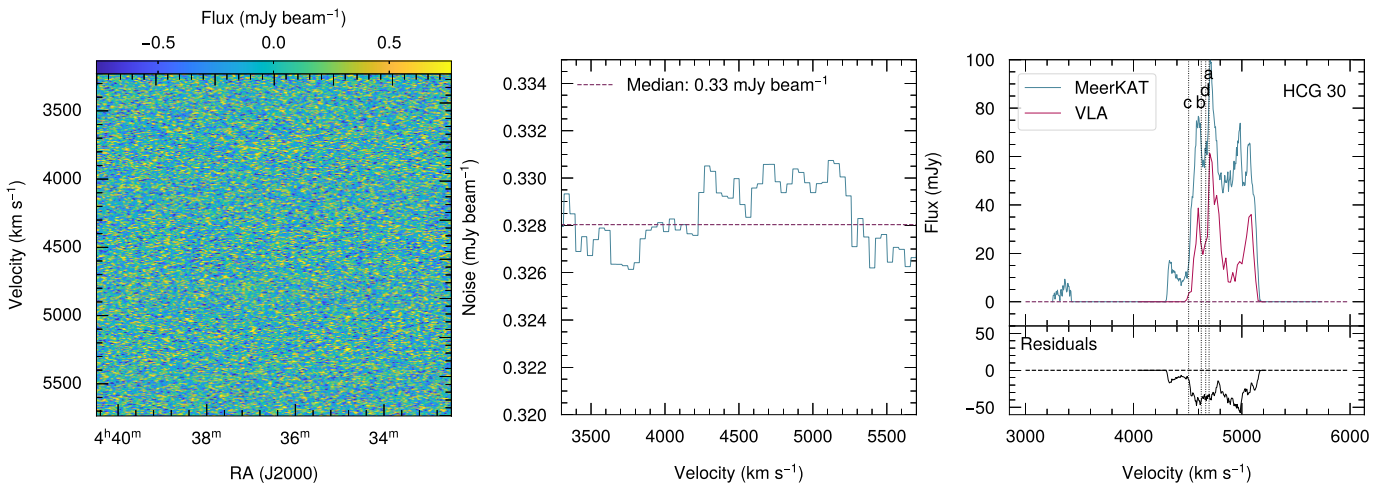


Fig. C.1: Left panel: velocity vs right ascension of HCG 30. Middle panel: median noise values of each RA-DEC slice of the non-primary beam corrected 60'' data cube of HCG 30 as a function of velocity. The horizontal dashed line indicates the median of all the noise values from each slice. Right panel: the blue solid lines indicates the MeerKAT integrated spectrum of HCG 30; the red solid line indicates VLA integrated spectrum of the group derived by (Jones et al. 2023). The vertical dotted lines indicate the velocities of the galaxies in the core of the group. The spectra have been extracted from areas containing only genuine H I emission.

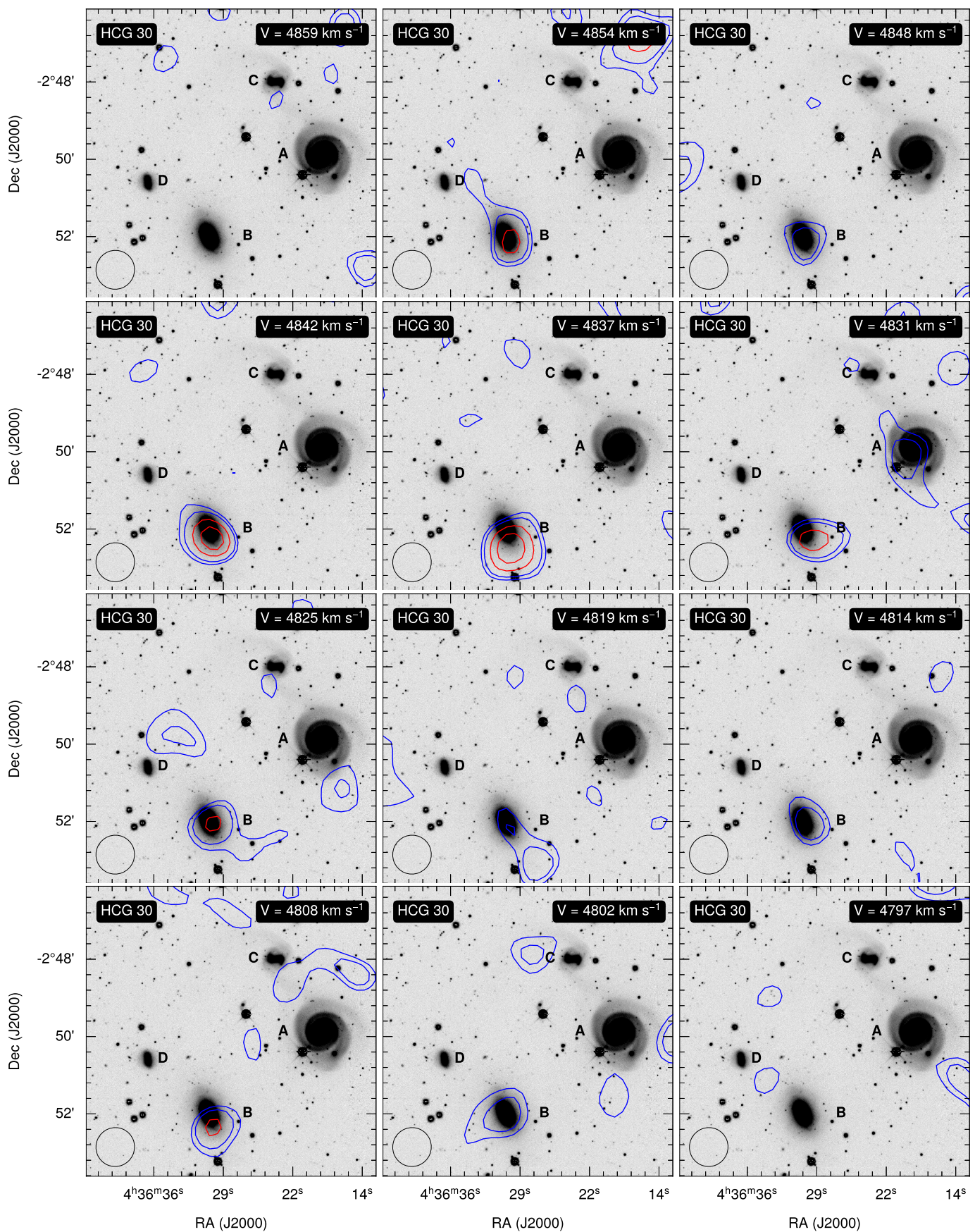


Fig. C.2: Example channel maps of the primary beam corrected cube of HCG 30 overlaid on DECaLS DR10 R-band optical image. Contour levels are (1.5, 2, 3, 4, 5, 6) times the median noise level in the cube (0.59 mJy beam<sup>-1</sup>). The blue colours show contour levels below 3σ; the red colours represent contour levels at 3σ, or higher. Additional channel maps can be accessed [online](#).

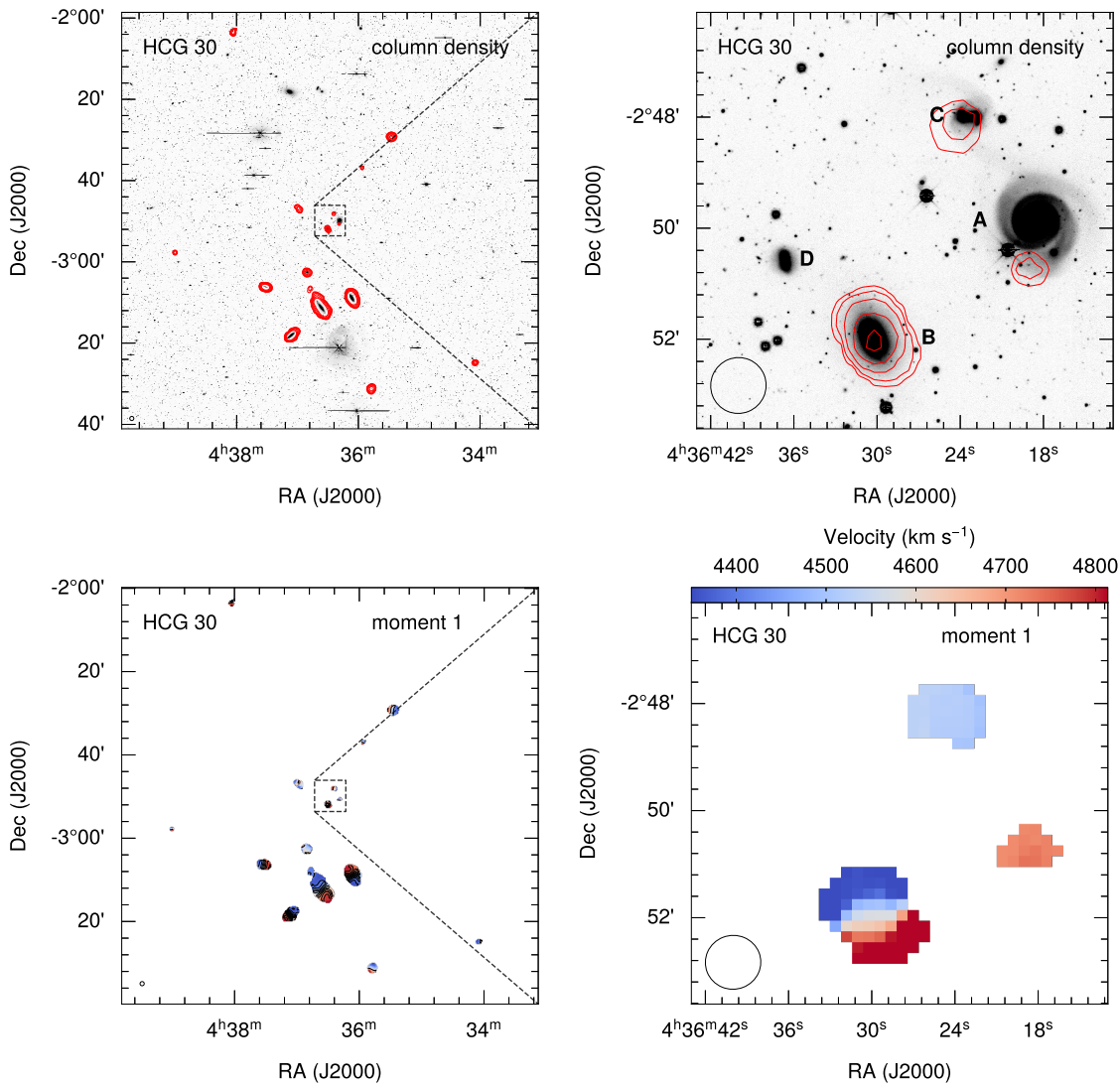


Fig. C.3: H I Moment maps of HCG 30. Left panels show all sources detected by SoFiA. The right panels show sources within the rectangular box shown on the left to better show the central part of the group. The top panels show the column density maps with contour levels of  $(6.0 \times 10^{18}, 1.2 \times 10^{19}, 2.4 \times 10^{19}, 4.8 \times 10^{19}, 9.6 \times 10^{19}, 1.9 \times 10^{20}) \text{ cm}^{-2}$ . The contours are overlaid on DECaLS DR10 R-band optical images. The bottom panels show the moment one map. Each individual source has its own colour scaling and contour levels to highlight any rotational component.

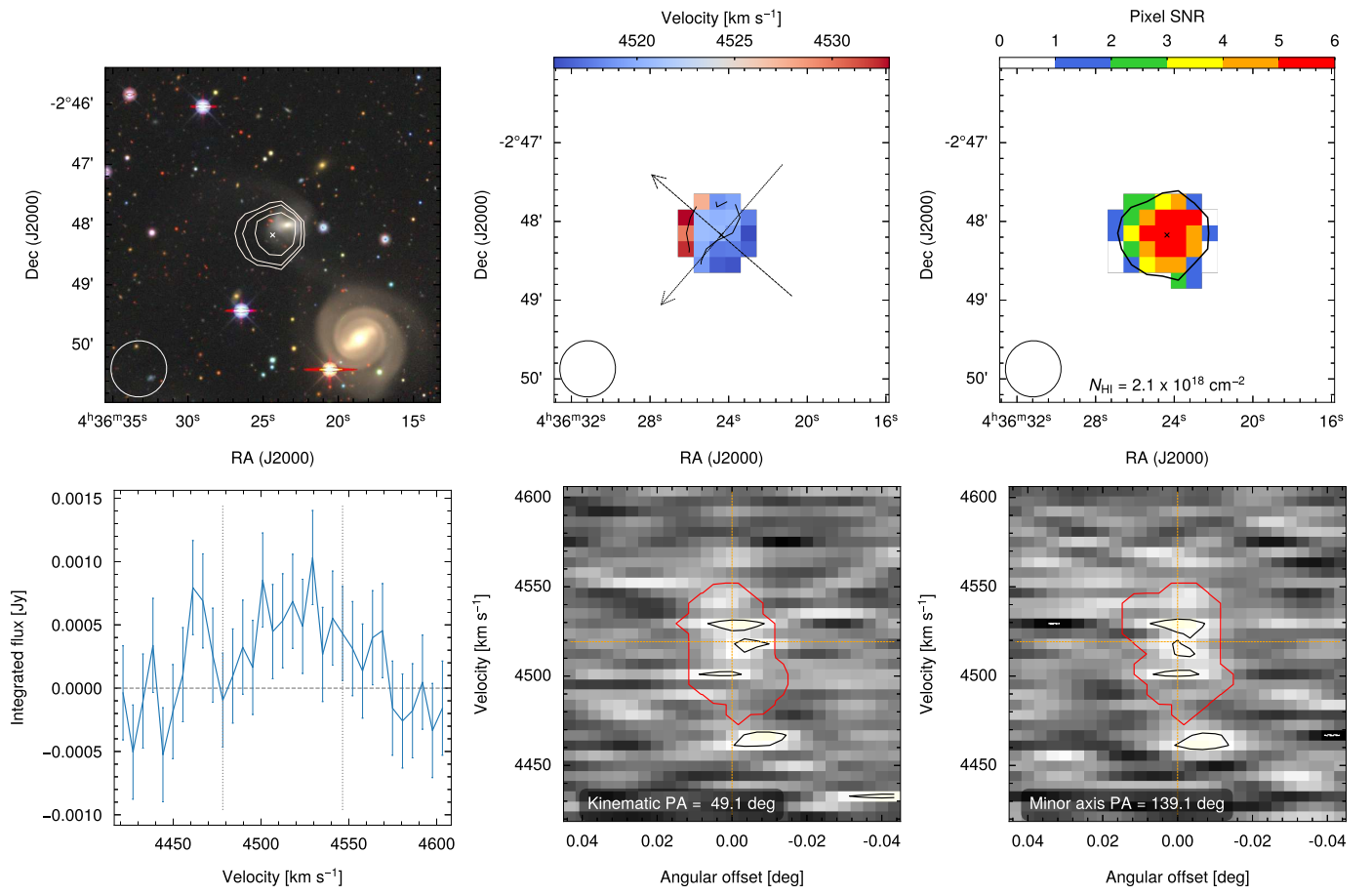


Fig. C.4: Top left: H I column density map overlaid on DECaLS optical image of HCG 30c. The contour levels are  $(2.10, 4.20, 8.41) \times 10^{18} \text{ cm}^{-2}$ . Top centre: moment-1 map. The arrows indicate the slices from which the position-velocity diagrams shown at the bottom panels were derived. Top right: signal-to-noise ratio map. Bottom left: global H I profile. Bottom centre: major axis position-velocity diagram. Bottom right: minor axis position-velocity diagram.

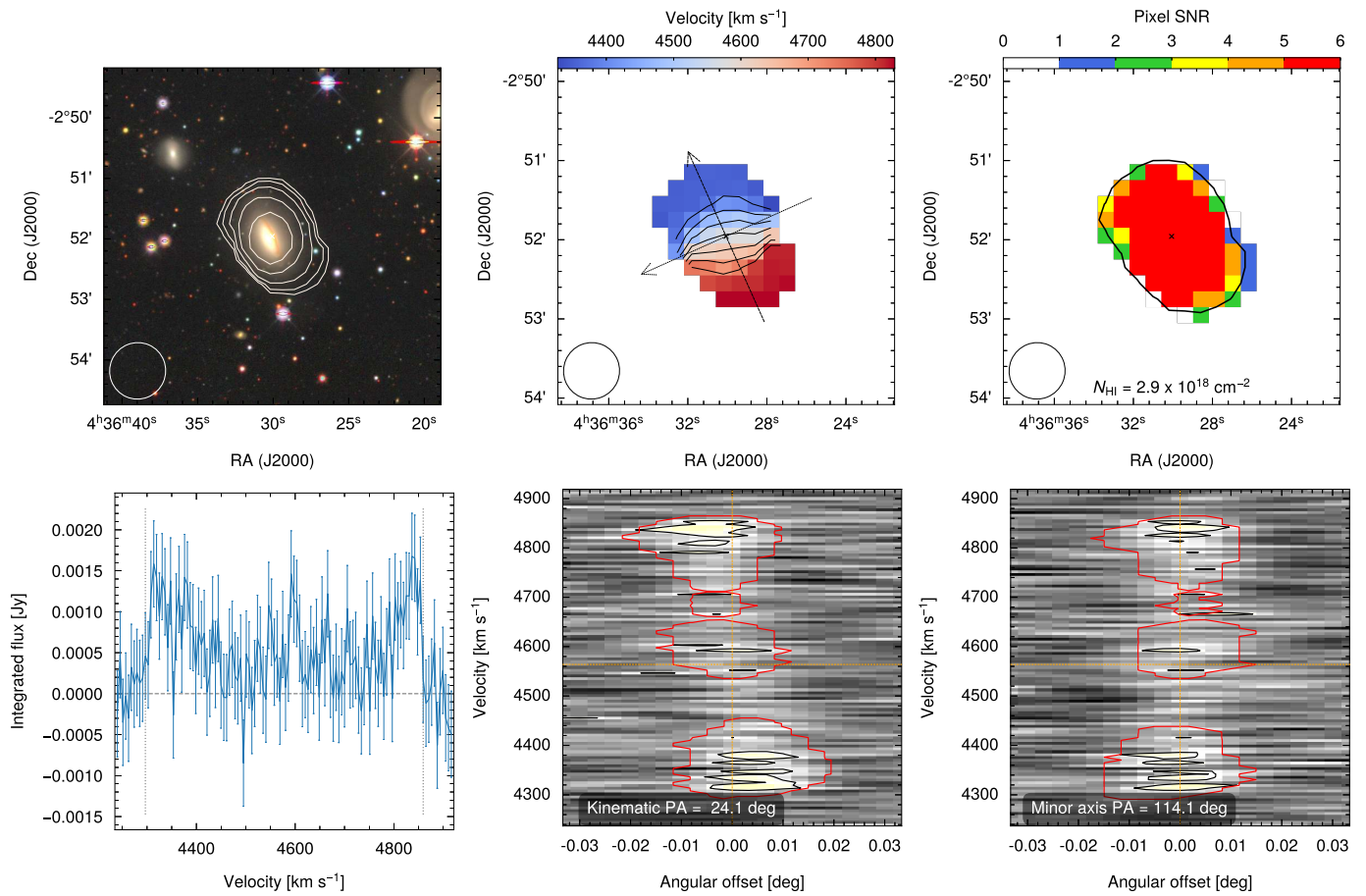


Fig. C.5: Top left: H I column density map overlaid on DECaLS optical image of HCG 30b. The contour levels are  $(0.29, 0.57, 1.14, 2.28, 4.57) \times 10^{19} \text{ cm}^{-2}$ . Top centre: moment-1 map, the contour levels are  $(4384, 4444, 4504, 4564, 4624, 4684, 4744) \text{ km s}^{-1}$ . The arrows indicate the slices from which the position-velocity diagrams shown at the bottom panels were derived. Top right: signal-to-noise ratio map. Bottom left: global H I profile. Bottom centre: major axis position-velocity diagram. Bottom right: minor axis position-velocity diagram.

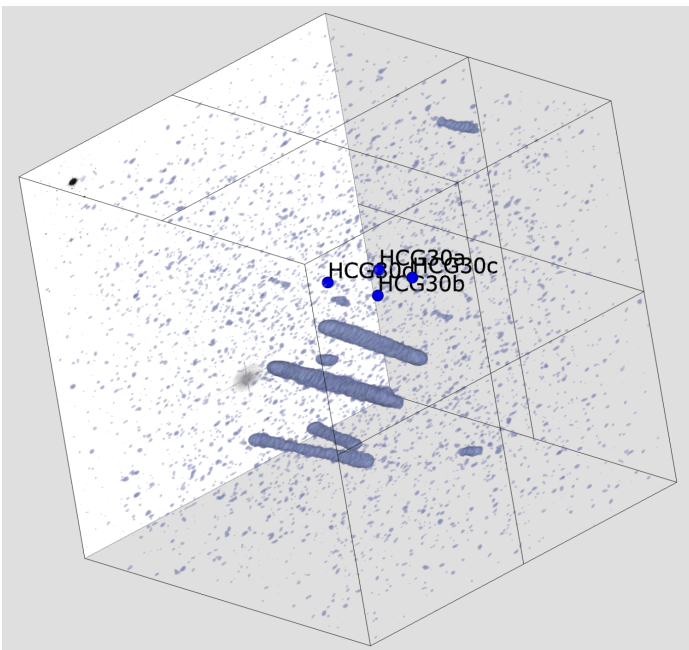


Fig. C.6: 3D visualisation of HCG 30. The blue circles indicate the position of the member galaxies. The 2D grayscale image is a DeCaLS R-band optical image of the group. The online version of the cubes are available at <https://amiga.iaa.csic.es/x3d-menu/>.

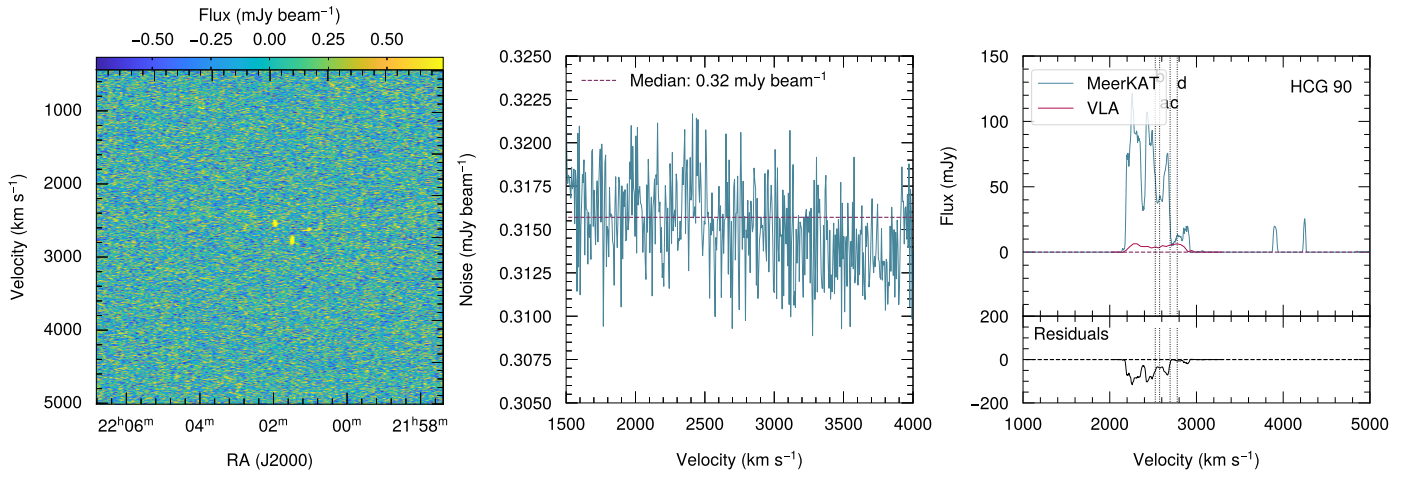


Fig. D.1: Left panel: velocity vs right ascension of HCG 90. Middle panel: median noise values of each RA-DEC slice of the non-primary beam corrected  $60''$  data cube of HCG 90 as a function of velocity. The horizontal dashed line indicates the median of all the noise values from each slice. Right panel: the blue solid lines indicates the MeerKAT integrated spectrum of HCG 90; the red solid line indicates VLA integrated spectrum of the group derived by (Jones et al. 2023). The vertical dotted lines indicate the velocities of the galaxies in the core of the group. The spectra have been extracted from areas containing only genuine H I emission.

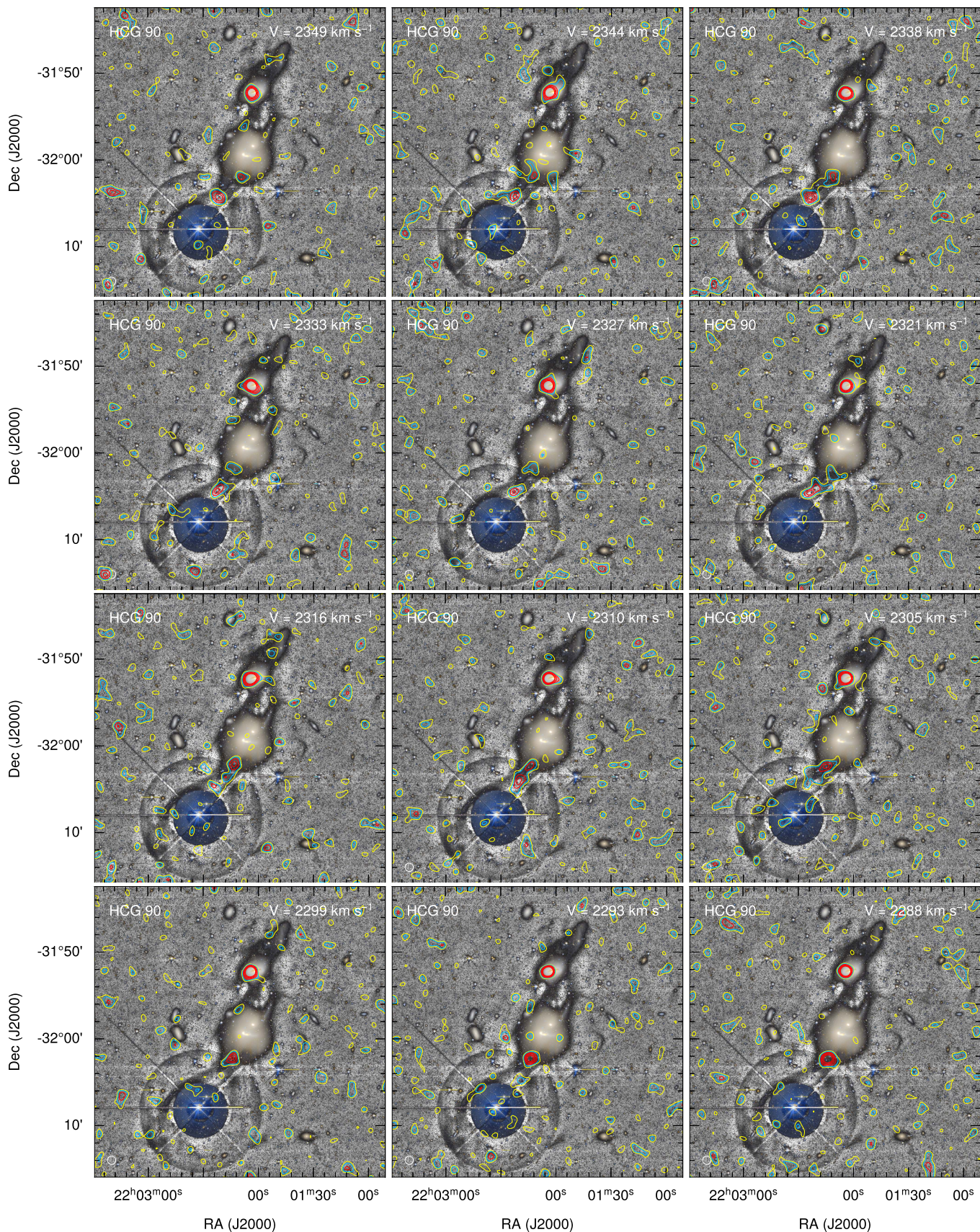


Fig. D.2: Example channel maps of the primary beam corrected cube of HCG 90 overlaid on enhanced DECaLS optical images. To improve the signal-to-noise ratio of the optical data and highlight the optical tail, we have added G-band and R-band images and aligned the pixel scale to  $8 \times 8$  ( $0.27 \times 8$  arcsec). Contour levels are (1.5, 2, 3, 4, 5, 6) times the median noise level in the cube ( $0.66 \text{ mJy beam}^{-1}$ ). The yellow and green colours show contour levels below  $3\sigma$ . The red colours represent contour levels at  $3\sigma$  or higher. Additional figures can be downloaded [here](#).



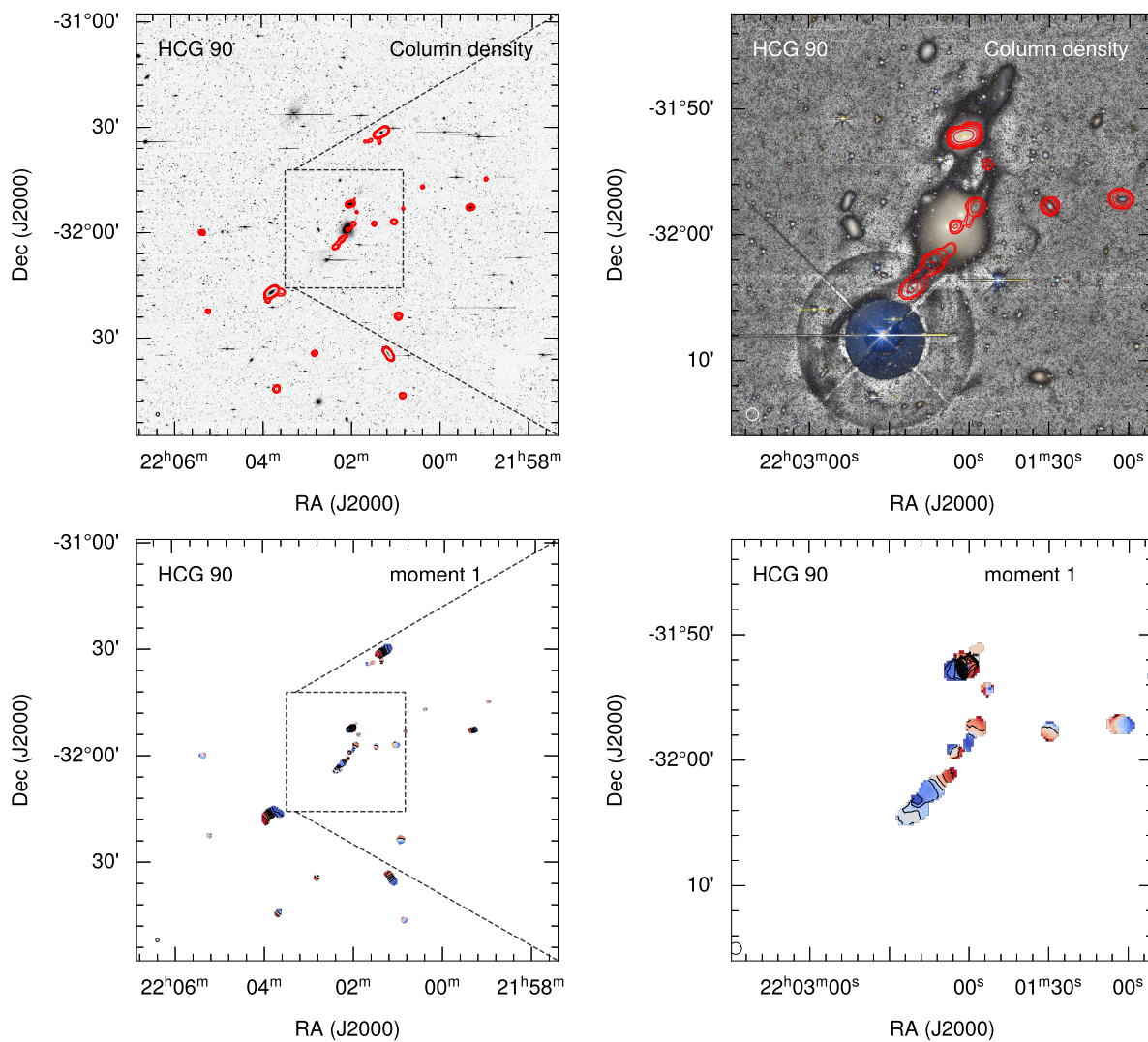


Fig. D.3: H I Moment maps of HCG 90. Left panels show all sources detected by SoFiA. The right panels show sources within the rectangular box shown on the left to better show the central part of the group. The top panels show the column density maps with contour levels of ( $3.9 \times 10^{18}$ ,  $7.7 \times 10^{18}$ ,  $1.5 \times 10^{19}$ ,  $3.1 \times 10^{19}$ ,  $6.2 \times 10^{19}$ ,  $1.2 \times 10^{20}$ ,  $2.5 \times 10^{20}$ )  $\text{cm}^{-2}$ . The contours are overlaid on DECaLS optical images. The bottom panels show the moment one map. Each individual source has its own colour scaling and contour levels to highlight any rotational component.

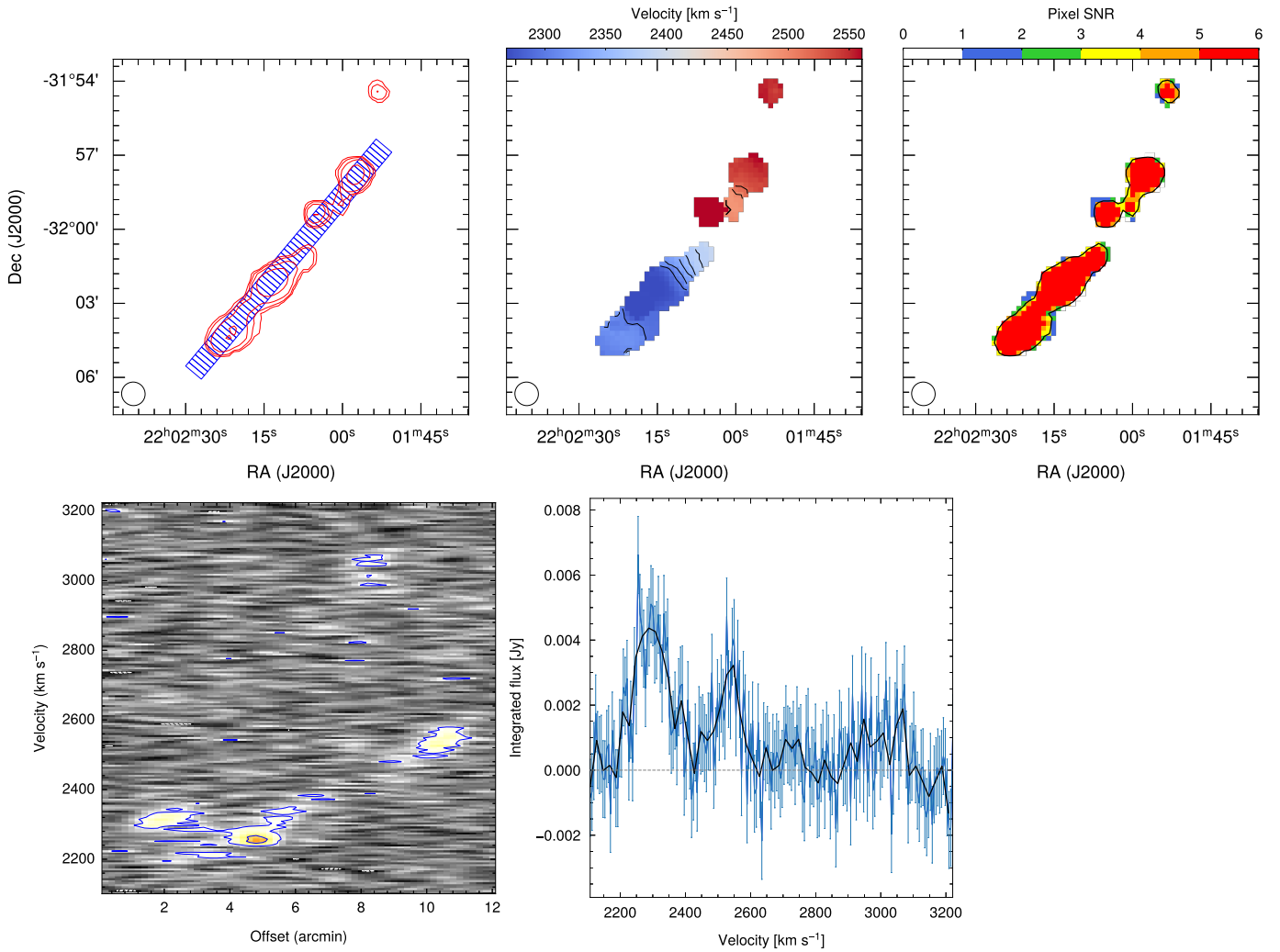


Fig. D.4: Top left: H I column density map of the tails of HCG 90. The contour levels are  $(0.35, 0.69, 1.38, 2.77) \times 10^{19} \text{ cm}^{-2}$ . The blue area indicates the slice from which the position-velocity diagram shown at the bottom panel was derived. Top centre: moment-1 map, the contour levels are  $(2300, 2320, 2340, 2360, 2380, 2400, 2420, 2440, 2460, 2480, 2500, 2520) \text{ km s}^{-1}$ . Top right: signal-to-noise ratio map. Pixels above  $6\text{-}\sigma$  are all shown in red. The black contour represent the lowest column density contour plotted at the top left panel of the figure. Bottom left: position-velocity diagram taken from the slice shown at the top right panel. Bottom right: global H I profile. The black line is a smoothed version of the profile using at  $20 \text{ km s}^{-1}$  velocity resolution.

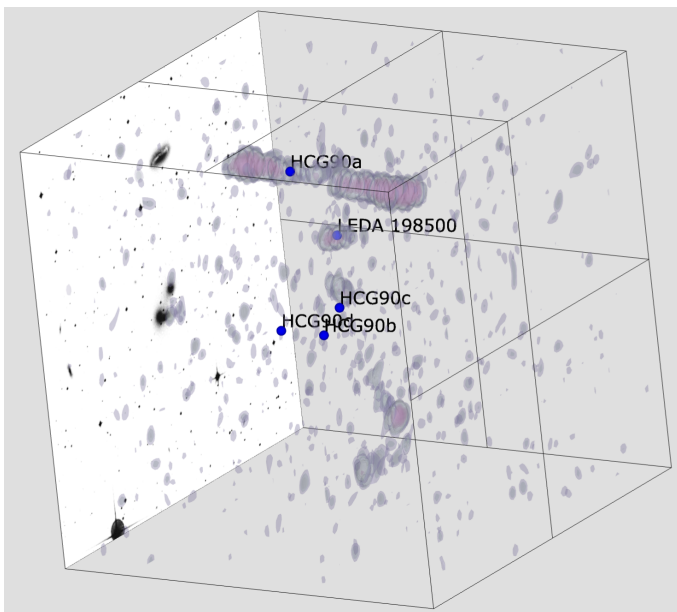


Fig. D.5: 3D visualisation of HCG 90. The blue circles indicate the position of the member galaxies. The 2D grayscale image is a DeCaLS R-band optical image of the group. The online version of the cubes are available at <https://amiga.iaa.csic.es/x3d-menu/>.

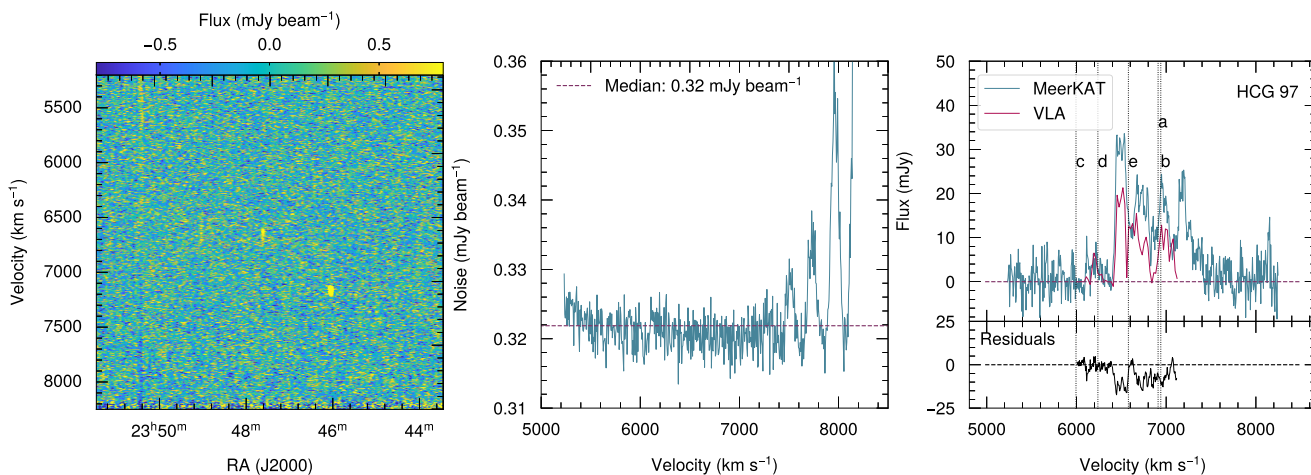


Fig. E.1: Left panel: velocity vs right ascension of HCG 97. Middle panel: median noise values of each RA-DEC slice of the non-primary beam corrected  $60''$  data cube of HCG 97 as a function of velocity. The horizontal dashed line indicates the median of all the noise values from each slice. Right panel: the blue solid lines indicates the MeerKAT integrated spectrum of HCG 97; the red solid line indicates VLA integrated spectrum of the group derived by (Jones et al. 2023). The vertical dotted lines indicate the velocities of the galaxies in the core of the group. The spectra have been extracted from areas containing only genuine H I emission.

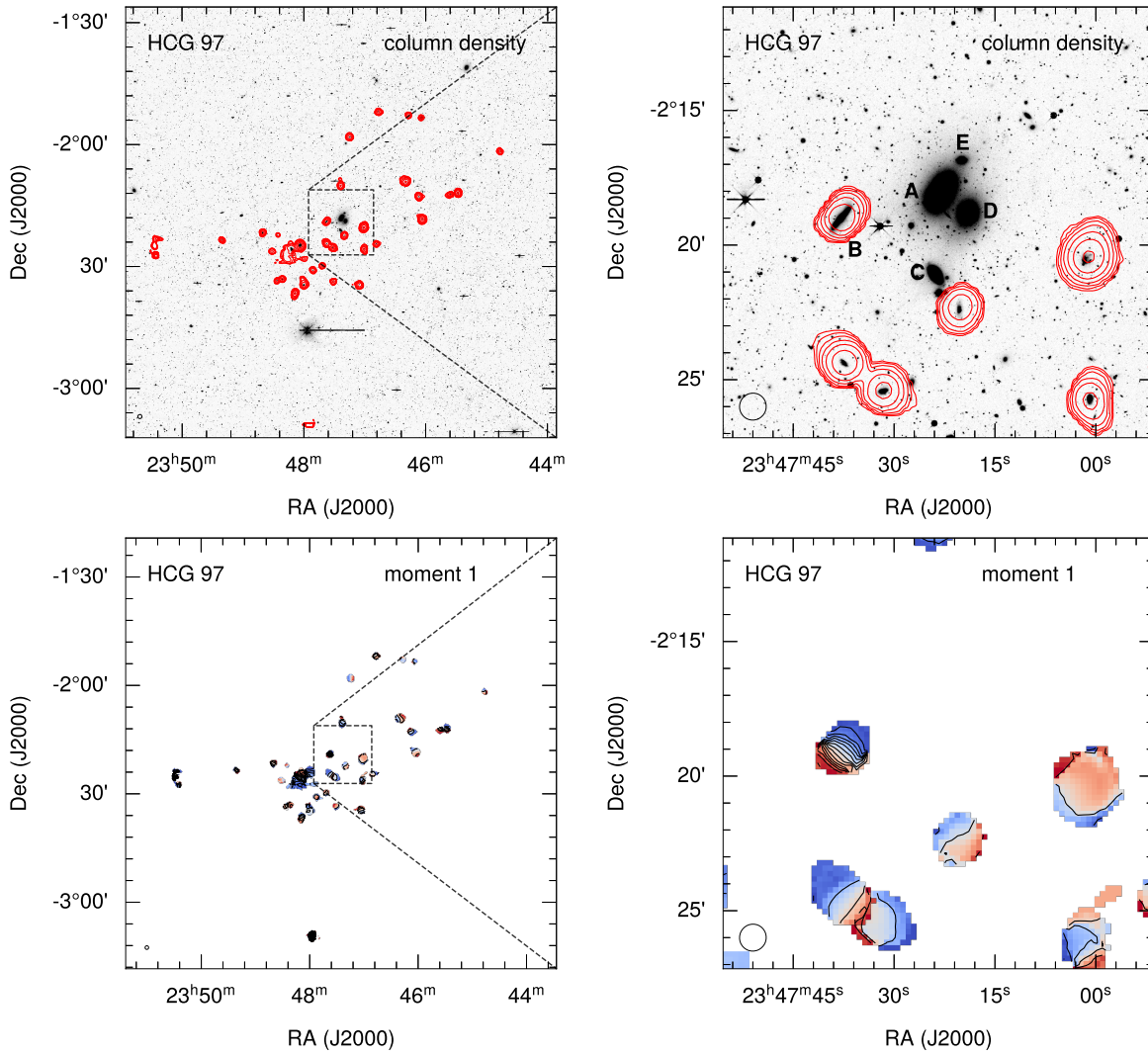


Fig. E.2: H I Moment maps of HCG 97. Left panels show all sources detected by SoFiA. The right panels show sources within the rectangular box shown on the left to better show the central part of the group. The top panels represent the column density map with contour levels of  $(3.5 \times 10^{18}, 7.0 \times 10^{18}, 1.4 \times 10^{19}, 2.8 \times 10^{19}, 5.6 \times 10^{19}, 1.1 \times 10^{20}, 2.2 \times 10^{20}) \text{ cm}^{-2}$ . The contours are overlaid on DECaLS R-band optical images. The bottom panels show the moment one map. Each individual source has its own colour scaling and contour levels to highlight any rotational component.

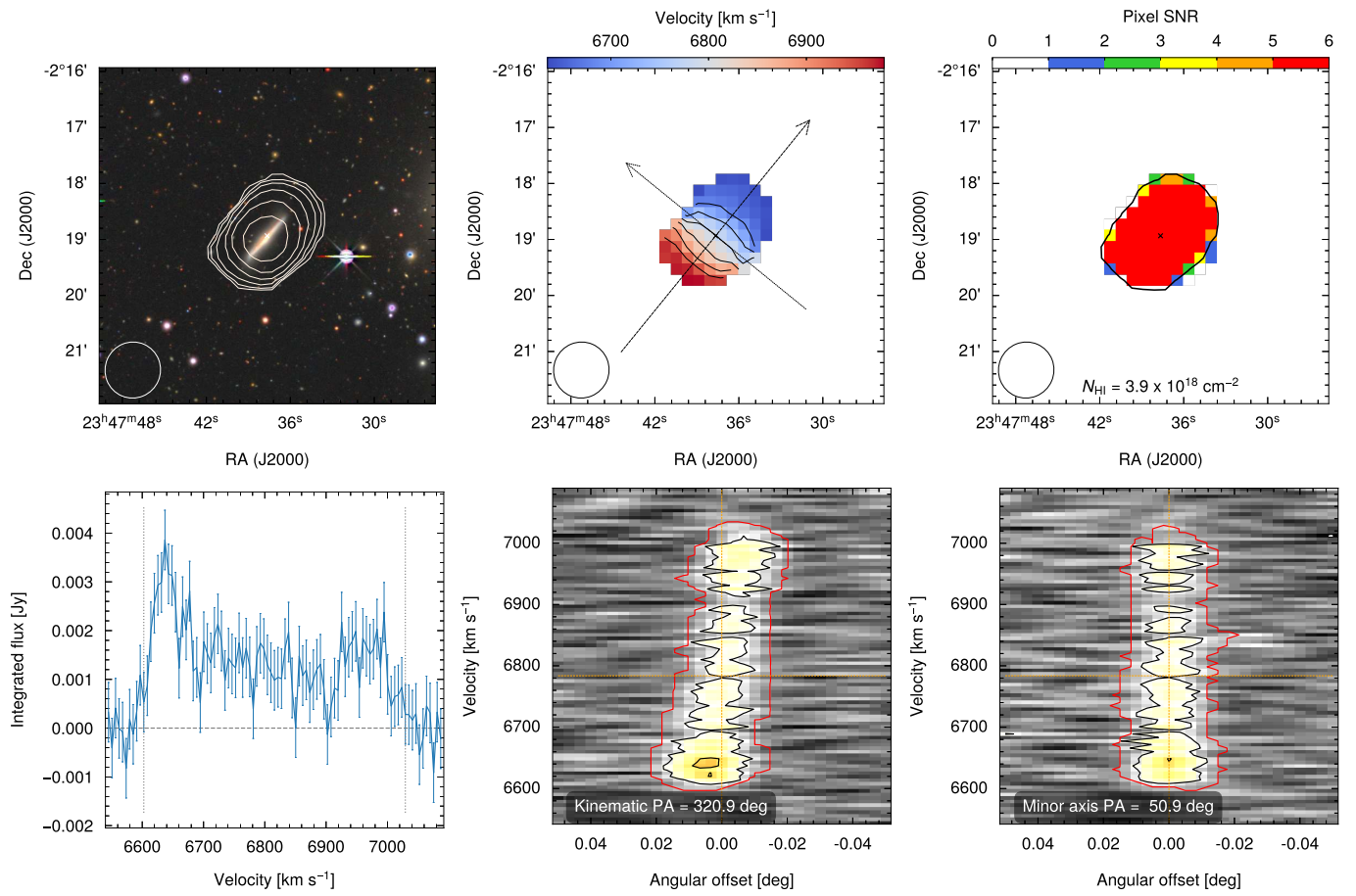


Fig. E.3: Top left: H I column density map overlaid on DECaLS optical image of HCG 97b. The contour levels are  $(2.10, 4.20, 8.41) \times 10^{18} \text{ cm}^{-2}$ . Top centre: moment-1 map. The arrows indicate the slices from which the position-velocity diagrams shown at the bottom panels were derived. Top right: signal-to-noise ratio map. Bottom left: global H I profile. Bottom centre: major axis position-velocity diagram. Bottom right: minor axis position-velocity diagram.

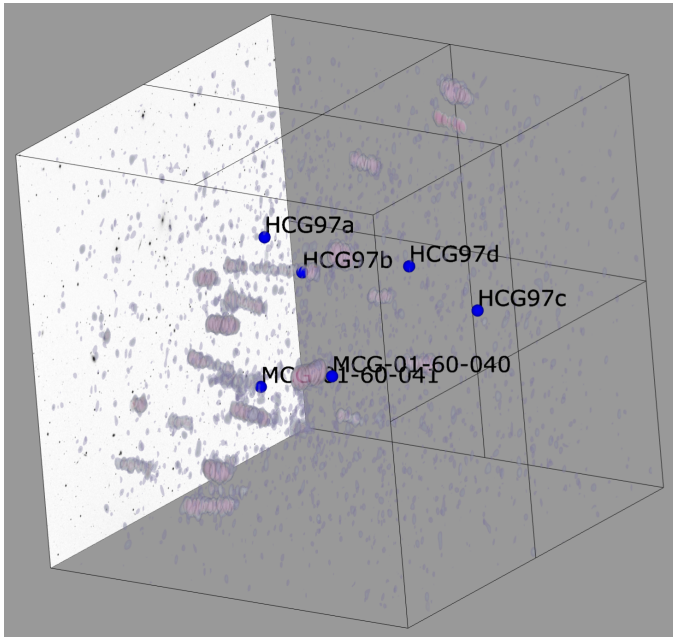


Fig. E.4: 3D visualisation of HCG 97. The blue circles indicate the position of the member galaxies. The 2D grayscale image is a DeCaLS R-band optical image of the group. The online version of the cubes are available at <https://amiga.iaa.csic.es/x3d-menu/>.